Rotor-Fuselage-Intake Aerodynamics and Icing Using Vortex and Eulerian-Lagrangian CFD Methods

Bidesh Sengupta[*], Esmaeil Esmaeilifar[*], M. Sadegh Araghizadeh[**], Sungu Kang[**], Hakjin Lee[††], Rho Shin Myong[‡]

[*, **, ††, ‡]School of Mechanical and Aerospace Engineering and ACTRC, Gyeongsang National University, Jinju, Gyeongnam 52828 South Korea

and

Lawrence Prince Raj[†]

[†]Department of Aerospace Engineering and Applied Mechanics, Indian Institute of Engineering Science and Technology, Shibpur, Howrah 711103, India

Abstract

Rotorcraft rotor-fuselage-intake aerodynamics and icing present unique challenges associated with rotor wake dynamics and the interaction of rotor wake with the fuselage and the intake. The effects of the rotor wake are dominant in low forward flight, and performing high-fidelity simulations of the rotor-fuselage-intake simultaneously is expensive. This study presents a novel hybrid nonlinear vortex-CFD approach to rotor-fuselage-intake aerodynamics and icing. The method combines nonlinear vortex-lattice, Lagrangian vortex-particle, and Eulerian CFD methods on airflow and droplet impingement with a PDE-based ice accretion model. The Lagrangian description of rotor wake preserves the wake structure independently of the Eulerian grid, while the Eulerian description of the flowfield naturally computes nonlinear flow phenomena and surface properties. The algorithm allowed the ice accretion to be computed much faster than existing methods. The method was validated by considering airflow, surface pressure, and ice accretion around a model rotorcraft. We investigated ice accretion with strong rotor wakes for different advance ratios and rotor thrust coefficients. We also investigated the effects of the suction of airflow in the intake and the differences between with and without the rotor. It was found that the advance ratio had a dominant effect compared to the rotor thrust coefficient.

Keywords: Aerodynamics, rotorcraft, forward flight, rotor wake, hybrid solver, ice accretion

---

[*]Research Fellow, School of Mechanical and Aerospace Engineering, 501 Jinjudaero, Gyeongnam.
[**]Graduate Student, School of Mechanical and Aerospace Engineering, 501 Jinjudaero, Gyeongnam.
[††]Assistant Professor, School of Mechanical and Aerospace Engineering, 501 Jinjudaero, Gyeongnam.
[‡] Professor, School of Mechanical and Aerospace Engineering and ACTRC, 501 Jinjudaero, Gyeongnam; myong@gnu.ac.kr. Associate Fellow AIAA (Corresponding Author).
[†]Assistant Professor, Department of Aerospace Engineering and Applied Mechanics, Shibpur, Howrah.

1. Introduction

Ice accumulates on the outer surfaces of rotorcraft, such as rotor blades and fuselage, when supercooled droplets collide during operation in a cold, humid environment. The accumulated ice changes the baseline geometry, drastically reducing the lift-to-drag ratio and, consequently, aerodynamic and propulsive performance [1, 2]. Serious aviation safety issues can also occur when the ice that has been shed from the blade surface is injected into the engine inlet or collides with the tail rotor blade [3-5].

Ice that has accumulated on the rotorcraft's fuselage can significantly reduce performance and jeopardize flight safety. Firstly, accreted ice on the engine inlet or nacelle deteriorates the flow quality, resulting in performance reduction. Additionally, the mass flow rate may be unexpectedly reduced, and an abrupt engine stall may occur when ice forms on foreign object damage (FOD) screens, which are designed to restrict the injection of debris. Secondly, ice accretion on the front fuselage’s windscreen can hinder the pilot’s vision, potentially leading to mission failure. Thirdly, significant ice buildup on sensors or communication devices may cause a loss of communication, or measurement error. In addition, the weight of the fuselage is increased by ice accretion, and the likelihood of mission failure increases with the increased weight of the helicopter [6]. Finally, an ice-accreted surface may undergo a substantial increase in drag. When the fuselage is subjected to icing conditions, it can increase surface roughness, leading to an increase in frictional drag [7-9]. Additionally, the ice geometry may result in a significant separation, which would have a negative impact on the helicopter’s maximum range and endurance.

While ice accretion on the fuselage affects the performance and airworthiness of a helicopter, there have been few studies on fuselage icing. Some recent studies have attempted to computationally predict ice accretion on helicopter fuselages and the associated performance degradation using numerical analysis tools and greater computing capacity. Having the ability to accurately predict ice accretion will enhance the design of ice protection systems [10-12].

Helicopter fuselages are situated below the rotors and are impacted by the rotor wake, unlike the flow fields of fixed-wing aircraft. To accurately predict ice accretion on the fuselage, rotor

inflow analysis is essential. The water droplet trajectory may alter as a result of the generated inflow from the rotor, which changes the locations where the droplets will collide with the fuselage. A droplet-trajectory analysis module and thermodynamic module are required to consider the three-dimensional (3-D) effects. Because the helicopter has a long slender rotor with a high aspect ratio, the 3-D effects are mainly confined to the rotor tip region. For this reason, it is acceptable to utilize approximate yet efficient methods such as the vortex lattice method for rotor blades. However, the same concept cannot be applied to the fuselage of a helicopter as it has 3-D effects.

Using the Lagrangian droplet-trajectory calculation module and the Euler equations, Szilder [13] attempted to predict the shape of the ice that would accrete on a Bell 412 helicopter fuselage without taking into account the influence of the rotors. Later, Szilder and Kozowski [14] expanded the study to take the rotor inflow into account, and they observed changes in droplet trajectory brought on by the rotor wake. Their study, however, relied on the Lagrangian droplet-trajectory module and the inviscid Euler equations. The Lagrangian-based droplet-trajectory module, as is widely known, has a built-in limitation: it is impossible to calculate the collection efficiency in the large separation zone since the released droplets cannot pass through the shadow region.

To investigate helicopter ice accretion, Aliga *et al*. [15] assumed that the flowfield was unsteady. The commercial code FENSAP-ICE was used to conduct a numerical analysis for a configuration with a two-bladed rotor and cylindrical fuselage (Georgia Institute of Technology model). FENCEP-ICE is based on the Navier-Stokes-Fourier equations for the flowfield analysis and the Eulerian droplet-trajectory module. Large amounts of computational power and time were needed to run the unsteady rotor and fuselage icing programs. They calculated the collection efficiency of the rotors and the fuselage at an instant in time. Applying the 3-D thermodynamic module to extract ice-accretion shapes proved exceedingly challenging.

By conducting an icing wind-tunnel test at the Centro Italiano Ricerche Aerospazilai and comparing the experimental results with the numerical results obtained from FENSAP-ICE, Ahn *et al*. [16] studied the ice shapes on a real-scale helicopter engine inlet model. The downwash caused by the rotor wake was not taken into account in detail in this investigation because the main goal was to determine the heat capacity of anti-icing devices.

The majority of previous studies did not take into account the impacts of the rotor wake when predicting ice accretion on the fuselage [13, 16]. The ice accretion was modeled for relatively high-speed forward flights [13], where the rotor-wake effects are minimal, even when the impacts of the rotor wake were taken into account. This was because performing simulations of the rotor and fuselage at the same time is expensive and time-consuming. However the effects of the rotor wake on the helicopter fuselage are dominant in low forward flight, and they should be considered to determine the correct ice shape under these flight conditions. Then, there have been theoretical problems with the numerical approaches used for the thermodynamic model and water-droplet trajectory. The Lagrangian method, which is commonly used for droplet-trajectory calculations, is unable to handle the separated flow region.

Fouladi *et al*. [17] conducted an ice-accretion analysis on a ROBIN (ROtor Body INteraction) model using the actuator disk model (ADM) in conjunction with the inflow model to identify rotor effects and the Eulerian droplet-trajectory module. The thermodynamic module was applied for various icing situations for forward flights with advance ratios of 0.15 and 0.23, and corresponding ice shapes were obtained. This model also underwent weight analysis and an aerodynamic performance study. Using Drees' linear inflow model [18], the thrust coefficient, which is a linear function of the radial and azimuthal positions on the rotor disk, was used to calculate the rotor inflow. They adversely impact the accuracy of the prediction of the droplet trajectories and flow field, because the detailed local characteristics caused by the interaction of tip vortices and inboard sheets with the fuselage cannot be included in this low-fidelity rotor-inflow model.

Son *et al*. [19] compared various actuator models, specifically the actuator surface model (ASM) [20], with the traditional ADM [21]. The reference line at which the induced velocities are measured can be fixed by using the ASM methodology. The ASM by Son *et al*. [19] was able to take into account unsteady flow in addition to modeling the production and propagation of tip vortices from each blade, whereas the ADM employed by Fouladi *et al*. [17] can only handle steady flow fields. Sengupta *et al*. [3] utilized the ASM methodology to compute the flow field around the rotorcraft. However, as the rotor wake is solved in the Eulerian framework, there is a requirement for high spatial discretization even further downstream of the rotor; otherwise,

numerical diffusion of the rotor wakes may be observed.

With this in mind, the current study makes an effort to establish an accurate prediction of the shape of the ice on the surface of the fuselage and the intake using up-to-date numerical techniques by combining Lagrangian and Eulerian frameworks for the aerodynamic solver [22-24]. The method combines the recently developed nonlinear vortex lattice method (NVLM), Lagrangian vortex particle method (VPM), and Eulerian unified CFD method of airflow and droplet impingement with a PDE-based ice accretion model. *The VPM part of the aerodynamic solver preserves the wake resolution even away from the rotorcraft independent of the Eulerian grid, hence tackling the limitation of wake numerical diffusion even with coarser grids.*

The novelties of the present hybrid method are summarized in Table 1, which compares modeling techniques for the rotor, rotor wake, and interaction between rotor wake and fuselage. Most previous studies took into account the effects of the rotor based on a simple model—imposing a pressure discontinuity across the rotor in terms of the boundary conditions, thus lacking a detailed wake physics—when predicting ice accretion on the rotorcraft fuselage. In this study, we present a novel hybrid method that computes the interaction between the rotor wake and the fuselage efficiently (at least 8.5 times), which plays a critical role in the airflow and ice accretion of the entire rotorcraft, for all advance ratios.

The rotor wake in the present method is modeled in the Lagrangian framework as wake particles, whereas the flow around the fuselage and the intake is modeled in the Eulerian framework. Then, these two methods are coupled to predict the flow field around the fuselage. As the rotor wakes are modeled in the Lagrangian framework, there is no requirement for high spatial discretization away from the rotor, and the rotor wakes are free from artificial numerical diffusion. The hybrid method requires low spatial discretization, making the method highly efficient both in terms of computational resources and time [23, 25, 26]. We also have conducted a full CFD simulation with overset methodology and have observed an acceleration of more than eight times, which is described in detail in section 3.1 (b). It will also be demonstrated in the 3.1 (b) subsection that when this method is applied to the ROBIN model rotorcraft, the pressure coefficients on the fuselage are predicted with reasonable accuracy compared to the experiment. The Eulerian

droplet-trajectory module and 3-D thermodynamic module enabled the efficient and precise prediction of ice accretion on the helicopter fuselage. The flow solver was validated using a GLC-305 wing [27].

A series of numerical calculations were carried out to investigate aerodynamics, droplet impingement, and ice accretion on the rotorcraft. The wake effects of the rotors on ice accretion under icing conditions were examined with various advance ratios and rotor thrust coefficients. The relationship between ice shape, advance ratio, and thrust coefficient was investigated in detail. Compared to the thrust coefficient, the advance ratio had the dominant effect on the boundaries of the fuselage exposed to the wake, which led to changes in the location and amount of ice accretion.

Table 1 Comparison of different methods available in the literature for rotorcraft icing

Features	H. Fouladi *et al*. (2013)	C. Son *et al*. (2017)	Present
Rotor modeling	Actuator disk method (ADM) coupled with the momentum equation	Actuator surface method (ASM) coupled with the momentum equation	Non-linear vortex lattice method (NVLM) coupled with the equations of density, momentum, and energy
Rotor wake modeling	Eulerian NSF CFD No explicit modeling	Eulerian NSF CFD No explicit modeling	Lagrangian VPM Explicit modeling
Blade characteristics	Neglects blade geometry	Blade as 2-D surface	Considers 3-D blade geometry (camber, swept angle)
Rotor-wake and wake-fuselage-intake interaction	Does not capture detailed rotor-wake interactions and vortices Does not consider air suction from the intake	Does not explicitly simulate the rotor-wake interactions Does not consider air suction from the intake	Accurately represents rotor-wake and wake-fuselage-intake interactions and vortices with unsteady effects
Airflow solver	Compressible NSF FEM solver	Compressible-PIMPLE segregated NSF FVM solver (OpenFOAM)	Compressible NSF Riemann-based FVM solver (In-house)
Computational efficiency	Relatively high computational efficiency	Moderate computational efficiency	Good balance between accuracy and computational efficiency

2. Computational methods

The icing analysis package developed for this work consists of four distinct modules, as illustrated in Fig. 1. They are namely: 1) Aerodynamic solver: to compute the flow field around

the rotorcraft; 2) Droplet solver: to compute droplet trajectory and deposition; 3) Ice accretion solver: thermodynamic solver to compute ice growth; and 4) Ice-shape generation solver: to compute final ice shape from ice growth. All of the modules were created in in-house code and the code was designed in such a way that there was very little user inconvenience when transferring data between them. Massive parallelism was achieved with OpenMPI-based parallel computing [28]. Although natural icing phenomena are highly unpredictable, this study assumed quasi-steady flows due to the limited computational resources. Droplet trajectories were obtained by solving droplet equations with the velocity vectors obtained from the converged solution of the aerodynamic flow field. Then, using these results, the icing simulations were performed. The ice shapes were obtained from the evaluation of the ice mass accreted on the surface.

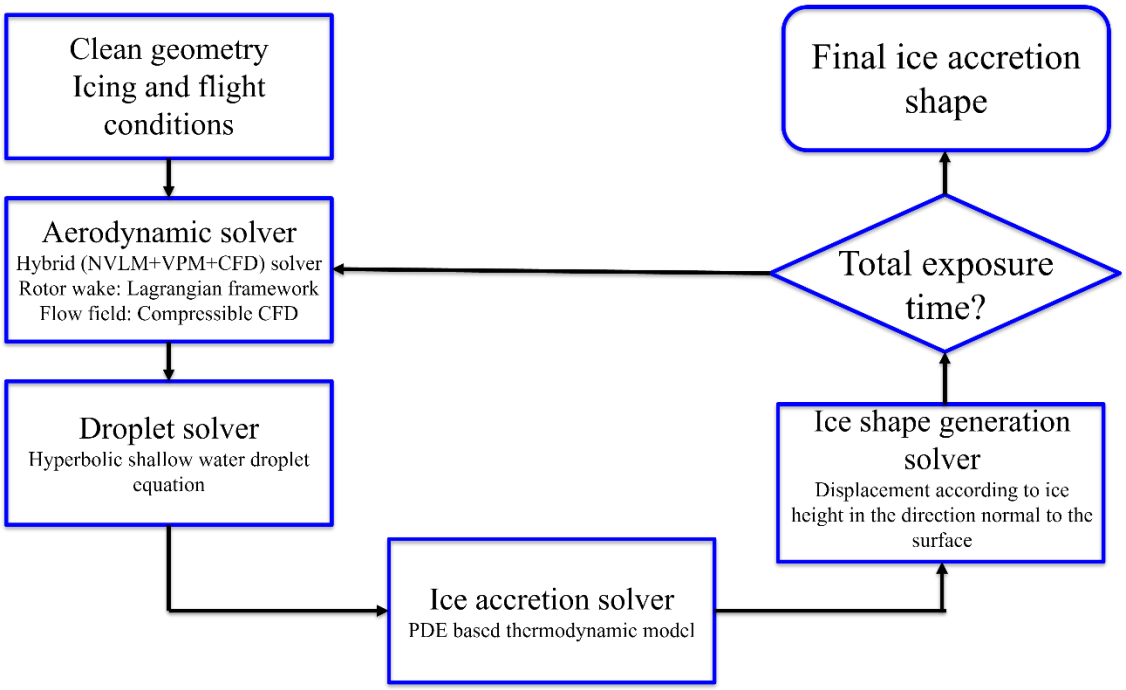

Fig. 1 Flow chart of the in-house ice accretion solver with different modules.

2.1. Aerodynamic solver: Hybrid (NVLM+VPM+CFD) compressible airflow solver

Vortex methods, such as the lifting line theory [18, 29-31], vortex lattice method [32-34], and the source-doublet panel method [35-37], help study rotor aerodynamics and simulate a full rotorcraft configuration, but they do not take viscosity and compressibility effects into account.

When the rotorcraft is operating in high-speed forward flight, these effects take precedence over the effect of rotor wake. At the same time, we can accurately simulate a variety of flow regimes using CFD methods, and we can also accurately depict the intricate flow dynamics that take place in the vicinity of rotor blades. Moreover, the accurate prediction of wall shear stress and heat flux required for icing simulations can be obtained accurately by CFD.

Taking advantage of both frameworks, the hybrid method consists of the nonlinear vortex lattice method (NVLM), vortex particle method (VPM), and Navier-Stokes-Fourier-based computational fluid dynamics (CFD) analysis model, where the NVLM, VPM, and CFD are used to, respectively, solve boundary vortices on the rotor blade, resolve the wake vorticity dynamics and calculate the near-body flow solution [23, 38-40].

Nonlinear vortex lattice method (NVLM)

The vortex lattice method (VLM) is one of the most efficient numerical approaches because it can represent wake vorticity fields without numerical dissipation error, and offer solutions with reasonable accuracy at low computing cost. VLM simulation, however, is unable to take nonlinear aerodynamic properties into account, which are mostly related to viscosity, flow separation, and low-Reynolds number flow. To mitigate these problems, Lee *et al*. [39-41] proposed the nonlinear vortex lattice technique (NVLM), which combines the VLM with vortex strength correction, airfoil lookup tables, and semi-empirical models.

VLM simulation provides accurate results at a reasonable computing cost for subsonic attached flow. The nonlinear aerodynamic behavior of rotor blades that take place at high angles of attack (above stalling or critical angles of attack) or low-Reynolds number flow, however, is not predicted by this model. The airfoil look-up table is a useful and efficient tool for obtaining aerodynamic data regarding rotor blade airfoils that are operating in attached and as well as stalled flow scenarios [42, 43]. In the NVLM/VPM simulation, the lift and drag coefficients are calculated at each blade section's control point using the sectional lookup table, which contains pre-calculated airfoil aerodynamic data for a wide range of Mach numbers and angles of attack. Additionally, NVLM and VPM are closely coupled to model unsteady wake dynamics. The

numerical algorithms employed in NVLM/ VPM are described in more detail [44-47].

The bound circulation strength of the rotor blade, which was calculated by solving a discretized linear system of equations (from Green's second identity for the solution of the Laplace equation), may have been overestimated [46-49]. According to Helmholtz's theorem, the vortex elements placed on the trailing edge of the rotor blades will shed into the wake during a time-marching simulation and have a constant strength. As a result, an erroneous calculation of the rotor wake geometry and evolution process might result in errors in induced velocity prediction, due to the overestimated strengths of boundary and wake vortices. Therefore, to obtain a more accurate solution, the effect of nonlinear aerodynamics on the boundary circulation strength should be taken into account. An iterative technique described by Lee *et al*. [39, 40] is utilized to obtain corrected and updated boundary vortices.

Vortex particle method (VPM)

In the current work, the geometry of the rotor wake is approximated by a finite number of vortex particles, which are shed from the whole width of the rotor blade. The strength of vortex particles is already determined at the previous time step by imposing the Kutta condition at the vortex elements placed on the trailing edges. Vortex particles naturally travel downstream with local convection velocity while being permitted to freely distort and interact with one another. The vorticity field in the wake is represented by a number of vortex particles as follows:

$$\boldsymbol{\omega}(\mathbf{x},t) = \sum_{i=1}^{n_p} \boldsymbol{\alpha}_i(t)\zeta_\sigma\left(\mathbf{x} - \mathbf{x}_i(t)\right), \tag{1}$$

$$\boldsymbol{\alpha}_i(t) = V_i\boldsymbol{\omega}_i(\mathbf{x}_i,t)\,. \tag{2}$$

Here, $\boldsymbol{\omega}(\mathbf{x},t)$ is the vorticity field in the wake, $\boldsymbol{\alpha}_i\,(t)$ is the strength vector, $\boldsymbol{\omega}_i(\mathbf{x}_i,t)$ is the vorticity vector and V_i is the volume of the i-th vortex particle. $\mathbf{x}$ is the position vector of an arbitrary point in the field, $\mathbf{x}_i$ is the position vector of the i-th vortex particle, and n_p is the number of vortex particles distributed in the field. The convection of the vortex particles is carried out by the following equation:

$$\frac{d\boldsymbol{x}}{dt} = \boldsymbol{u}_{tot} = \boldsymbol{u}_\infty + \boldsymbol{u}_{vpm}\,. \tag{3}$$

The detailed derivation and description of VPM can be found in the previous works [50-52].

Coupling of NVLM, VPM, and CFD

The coupled VPM/CFD simulation consists of applying VPM to resolve the wake vorticity dynamics and an unstructured CFD solver to compute the near-body flow solution. VPM is used to solve the dynamics of wakes emanating from the rotors, wings, etc., convect the wake vorticity under the combined influence of the free stream, and account for self-induced wake velocities and flow field disturbances due to bodies, such as the fuselage. The CFD solver is used to compute the flow field around the bodies, which includes the effect of rotor wake-induced velocities and provides a modified flow field disturbance to the VPM wake solution.

The vortex particle dynamics are then governed by a convection process, as follows:

$$\frac{d\boldsymbol{x}}{dt} = \boldsymbol{u}_{tot} = \boldsymbol{u}_{\infty} + \boldsymbol{u}_{vpm} + \Delta\boldsymbol{u}_{cfd} \,. \tag{4}$$

As a high-fidelity near-body flow solver, the Navier-Stokes-Fourier CFD method is applied to fully capture nonlinear flow phenomena from the first principles. Allowing for the effect of the VPM wake-induced velocity, the governing equation of the near-body CFD solver can be modified as follows:

$$\frac{\partial}{\partial t}\iiint_{V} \boldsymbol{W}\, dV + \iint_{S} \left(\boldsymbol{F}_i - \boldsymbol{F}_v + \Delta\boldsymbol{F}\left(\boldsymbol{u}_{vpm}, \boldsymbol{u}_{cfd}\right)\right) dS = 0 \,. \tag{5}$$

Here $\boldsymbol{W}$ is the flow state variable; $\boldsymbol{F}_i$ and $\boldsymbol{F}_v$ are the inviscid and viscous fluxes, respectively; V is the fluid domain considered; S is the boundary of the fluid domain; and $\boldsymbol{n}$ is the normal vector pointing into the fluid domain. To account for the VPM-induced velocity, a flux correction term, $\Delta\boldsymbol{F}(\boldsymbol{u}_{vpm}, \boldsymbol{u}_{cfd})$, is introduced. Because of the coupled solution, the flux correction depends on both the VPM-induced velocity field and the CFD solver velocity field. For compressible flow, $\boldsymbol{W}$ is presented as:

$$\boldsymbol{W} = \begin{bmatrix} \rho \\ \rho u_{cfd} \\ \rho v_{cfd} \\ \rho w_{cfd} \\ \rho E \end{bmatrix}. \tag{6}$$

Here $\boldsymbol{u}_{cfd} = (u_{cfd}, v_{cfd}, w_{cfd})$ is the CFD solved flow velocity states; p is the state variable for pressure, and ρ and E are state variables for density and total energy.

The "Flux Correction Approach" [22, 24] can be conveniently applied to account for the VPM-induced velocity in the unstructured CFD solvers. In the implementation, the VPM-induced velocity contributes to the correction of the convective flux term in the CFD solver. The correction terms due to the VPM-induced velocity can be formatted as:

$$\Delta \boldsymbol{F}\left(\boldsymbol{u}_{vpm}, \boldsymbol{u}_{cfd}\right) = \begin{bmatrix} \rho \boldsymbol{u}_{vpm} \cdot \boldsymbol{n} \\ \rho u_{cfd} \boldsymbol{u}_{vpm} \cdot \boldsymbol{n} \\ \rho v_{cfd} \boldsymbol{u}_{vpm} \cdot \boldsymbol{n} \\ \rho w_{cfd} \boldsymbol{u}_{vpm} \cdot \boldsymbol{n} \\ \rho E \boldsymbol{u}_{vpm} \cdot \boldsymbol{n} \end{bmatrix} \tag{7}$$

where $\boldsymbol{u}_{vpm}$ is the VPM-induced velocity field. The convective flux $\boldsymbol{F_i}$ and viscous flux $\boldsymbol{F_v}$ are given by:

$$\boldsymbol{F}_i = \begin{bmatrix} \rho \boldsymbol{u}_{cfd} \cdot \boldsymbol{n} \\ \rho u_{cfd} \boldsymbol{u}_{cfd} \cdot \boldsymbol{n} + n_x p \\ \rho v_{cfd} \boldsymbol{u}_{cfd} \cdot \boldsymbol{n} + n_y p \\ \rho w_{cfd} \boldsymbol{u}_{cfd} \cdot \boldsymbol{n} + n_z p \\ \rho H \boldsymbol{u}_{cfd} \cdot \boldsymbol{n} \end{bmatrix}, \ \boldsymbol{F}_v = \begin{bmatrix} 0 \\ \boldsymbol{\tau}_x \cdot \boldsymbol{n} \\ \boldsymbol{\tau}_y \cdot \boldsymbol{n} \\ \boldsymbol{\tau}_z \cdot \boldsymbol{n} \\ (\boldsymbol{\tau} \cdot (\boldsymbol{u}_{cfd} + \boldsymbol{u}_{vpm}) + \boldsymbol{Q}) \cdot \boldsymbol{n} \end{bmatrix}. \tag{8}$$

Here, H is the enthalpy. The non-conserved variables $\boldsymbol{\tau}$ and $\boldsymbol{Q}$ denote the viscous shear stress tensor and the heat flux, respectively.

$$\begin{aligned} \boldsymbol{\tau} &= 2\eta \left[\nabla \boldsymbol{u}_{tot}\right]^{(2)}, \\ \boldsymbol{Q} &= k \nabla T \ . \end{aligned} \tag{9}$$

The symbol $[A]^{(2)}$ in the shear stress tensor stands for the traceless symmetric part of the tensor A. The η and k are the viscosity and thermal conductivity, respectively, and are dependent on the

air temperature.

In any numerical simulation, the boundary condition has a significant effect on the convergence, stability, and accuracy of the solution. Hence modeling the boundary is not a trivial task, due to the truncation of the real physical domain. The boundary conditions applied for the current coupled Navier-Stokes-Fourier equations are as follows:

Solid surface: In the fully coupled VPM/CFD solver, the boundary condition on the body surfaces needs to be correspondingly modified. On the body surfaces, the flow velocity will be the same as the body velocity due to the viscosity effect. In the VPM/CFD coupling, the no-slip boundary condition was enforced so that the combined velocity field, $\boldsymbol{u}_{cfd} + \boldsymbol{u}_{vpm}$, is the same as the body velocity, $\boldsymbol{u}_{body}$, as follows:

$$\boldsymbol{u}_{cfd} + \boldsymbol{u}_{vpm} = \boldsymbol{u}_{body} . \tag{10}$$

For a stationary body ($\boldsymbol{u}_{body}$), the no-slip boundary condition for the VPM/CFD coupling becomes $\boldsymbol{u}_{cfd} = -\boldsymbol{u}_{vpm}$.

Far-field: Similarly, in the outer boundary of the CFD grid, the far-field boundary condition needs to be imposed. Typically, the far-field boundary condition can be enforced based on Riemann invariants. To account for the effect of the VPM rotor wake on the CFD far-field boundary, the far-field Riemann boundary condition can be modified to handle the VPM/CFD coupling. When the flow at the local grid has outgoing characteristics, the flow state on the boundary will be extrapolated from the inner CFD grid nodes. When the flow at the local grid has incoming characteristics, the flow state on the boundary will take the combined values from both the free stream value and the VPM-induced velocity data. For an incompressible flow, the "free stream" state is written as:

$$\begin{aligned} p_{far} &= \frac{1}{2}[\, p_{free} + p_{\text{int}} - \rho_0 c_0 [n_x - 0.5(u_{\text{int}} + u_{vpm})) + \\ & n_y (v_{free} - 0.5(v_{\text{int}} + v_{vpm})) + n_z (w_{free} - 0.5(w_{\text{int}} + w_{vpm})), \\ \rho_{far} &= \rho_{free} + (p_{far} + p_{free}) / c_0^2, \\ u_{far} &= u_{free} - n_x (p_{free} - p_{far}) / \rho_0 c_0, \\ v_{far} &= v_{free} - n_x (p_{free} - p_{far}) / \rho_0 c_0, \end{aligned} \tag{11}$$

$$w_{far} = w_{free} - n_x (p_{free} - p_{far}) / \rho_0 c_0.$$

Here, the subscripts *free*, *int* and *vpm* denote freestream, cell center value of the boundary cell, and quantities obtained from vortex particles, respectively.

The algorithm for the hybrid aerodynamic solver in which blade and wake are solved by NVLM and VPM, and then the flow field around the fuselage is solved using CFD is performed for each time step, as described in Fig. 2. The steps are as follows:

(a) Define the initial configuration, rotor model, and blade discretization before starting the simulation.

(b) Start running the NVLM/VPM module to generate a wake from the rotor.

(c) Calculate the induced velocities on each cell center of the CFD grid due to wake particles.

(d) Compute the flux correction term as given in Eq. (7) from the induced velocities at cell centers, obtained from wake particles.

(e) Run the CFD simulation to solve the equation given in Eq. (5) to compute conservative variables as given in Eq. (6).

(f) Map the velocities obtained from the CFD grid to the nearest wake particles. Here, this operation was achieved by kd-tree.

(g) Let the wake downstream convect according to the wake convection equation, given by Eq. (4).

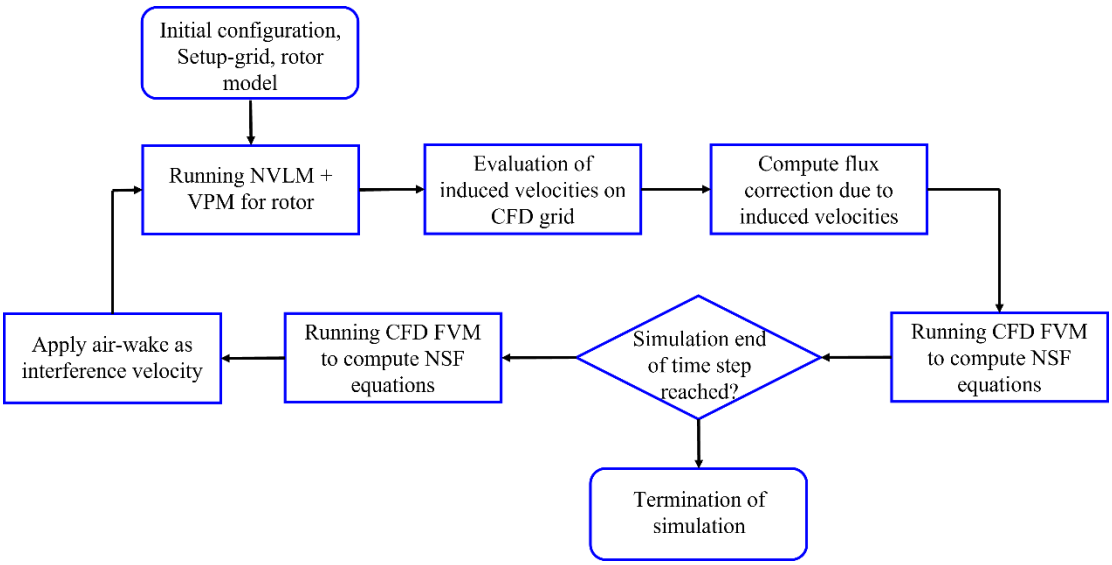

Fig. 2 Flow chart of the hybrid aerodynamic solver.

2.2. Droplet solver

A computational method based on the Lagrangian [53, 54] or Eulerian [55-57] methods is usually used to predict droplet impingement. The Lagrangian droplet tracking method has some limitations, especially for cases where complex geometries are involved. This method has difficulty solving multi-element airfoils, non-axisymmetric models, and systems involving both external and internal flows. In addition, for three-dimensional models, the computation for the Lagrangian method is extremely expensive and complex. On the other hand, the Eulerian method can handle all these issues without much difficulty.

In the Eulerian droplet method, the dispersed phase is considered a continuum, and continuity and momentum equations are solved to predict the droplet distributions. Since the mass loading ratio of the bulk density of the droplets over the bulk density of air is on the order of 10^{-3} in air-droplet flows, the two-phase flow can be simulated using a weakly coupled (one-way coupling) algorithm. The airflow data should then be provided to the droplet solver through the source terms for the Eulerian droplet equations [56].

A Eulerian-based shallow water-type droplet equation (SWDE) [57, 58] is employed for the present droplet solver. The conservative form of SWDE can be written as,

$$\begin{bmatrix} \rho \\ \rho \boldsymbol{u} \end{bmatrix} + \nabla \cdot \begin{bmatrix} \rho \boldsymbol{u} \\ \rho \boldsymbol{u}\boldsymbol{u} + \rho g d \mathbf{I} \end{bmatrix} = \begin{bmatrix} 0 \\ \mathbf{S}_D + \mathbf{S}_G + \mathbf{S}_S \end{bmatrix} \tag{12}$$

where,

$$\boldsymbol{S}_D = \begin{bmatrix} 0 \\ A_u\left(u_g - u\right) \\ A_v\left(v_g - v\right) \\ A_w\left(w_g - w\right) \end{bmatrix}, \boldsymbol{S}_G = \begin{bmatrix} 0 \\ 0 \\ 0 \\ 1 - \rho_g / \rho_w \end{bmatrix}, \boldsymbol{S}_S = \begin{bmatrix} 0 \\ \left(\rho g d\right)_x \\ \left(\rho g d\right)_y \\ \left(\rho g d\right)_z \end{bmatrix}. \tag{13}$$

Here, ρ is the density of droplets in terms of liquid water content (LWC). Also, u, v and w are the velocity components of the $x, y,$ and z directions, respectively. $\boldsymbol{S}_D, \boldsymbol{S}_G$ and $\boldsymbol{S}_S$ are the aerodynamic drag, gravity, and buoyancy forces acting on the droplets and added source terms, respectively.

The $\boldsymbol{S}_D$ denotes the drag on droplets caused by the airflow. The $\boldsymbol{S}_G$ and $\boldsymbol{S}_S$ terms denote the resulting force of gravity and the buoyancy of the droplets. The density of air and water is given by ρ_g and ρ_w respectively. u_g, v_g and w_g are the velocities of gas in each direction, respectively, and g is the acceleration due to gravity. The coefficients $\boldsymbol{A}_{u,v,w}$ can be expressed as

$$\boldsymbol{A}_{u,v,w} = A_u = 0.75\rho C_{D_u} \mathrm{Re}_u \, \mu / \rho_w d^2, \mathrm{Re}_u = \rho_u d \left| \boldsymbol{u}_g - \boldsymbol{u} \right| / \mu \tag{14}$$

where Re_u is the Reynolds number of the droplets, μ is the dynamic viscosity of the gas, and C_D is the drag coefficients of the spherical droplets. The drag coefficient [58] can be derived as follows,

$$C_{D_u} = \begin{cases} \dfrac{24}{\mathrm{Re}_u}\left(1 + 0.0197\,\mathrm{Re}_u^{0.63} + 2.6e-4\,\mathrm{Re}_u^{1.38}\right), \text{ if } \mathrm{Re}_u < 100 \\ 0.4, \text{ if } \mathrm{Re}_u > 1000 \end{cases} \tag{15}$$

The details of the spatial discretization of the droplet equations were given by Jung *et al*. [57].

The boundary condition plays a very important role in the accuracy and convergence of any numerical simulations. Special attention is necessary for the SWDEs, to impose the solid wall boundary condition. Generally, droplet solvers provide droplet distribution around the given geometry, and it is necessary to know the collection efficiency. The collection efficiency is a non-dimensional quantity used to measure the potential of ice accretion and is based on droplet volume fraction (α), free stream droplet volume fraction (α_∞), the velocity (**u**), free stream velocity (u_∞), and the normal vector on the solid surface. It can be expressed as,

$$\beta = \frac{-\alpha \mathbf{u} \cdot \mathbf{n}}{\alpha_\infty u_\infty}. \tag{16}$$

Therefore, setting the solid surface condition is an important factor in the solution of droplet flow fields.

In the present work, a permeable wall boundary condition [60, 61] is employed for the droplet impingement. Under this boundary condition, the droplets will collide once the projection of a normal vector on a solid surface and the droplet velocity in an adjacent cell on the solid surface is negative. This behavior of droplets at the wall boundary can be implemented numerically, as follows,

$$\begin{aligned} \mathbf{u}_{wall} &= \mathbf{u} \quad \text{if} \quad \mathbf{u}\cdot\mathbf{n} \le 0, \\ \mathbf{u}_{wall} &= 0 \quad \text{if} \quad \mathbf{u}\cdot\mathbf{n} \ge 0. \end{aligned} \tag{17}$$

2.3. Ice accretion solver

The ice accretion solver was developed using the Messinger model [62], in particular, based on a partial differential equation (PDE) formulation instead of the commonly used control volume method [63]. A PDE-based ice accretion model [64] was introduced that uses the mass balance and energy equation. These equations are called the shallow water icing model [65], which assumes a linear velocity profile to liquid film on the surface.

$$\rho_w \left[\frac{\partial h_f}{\partial t} + \vec{\nabla}\cdot\left(\bar{u}_f h_f\right) \right] = U_\infty LWC_\infty \beta - \dot{m}_{evap} - \dot{m}_{ice}, \tag{18}$$

$$\begin{aligned} \rho_w C_{p,w} \left[\frac{\partial h_f T_{equi}}{\partial t} + \nabla\cdot\left(\bar{u}_f h_f T_{equi}\right) \right] &= \left[C_{p,w}\tilde{T}_{d,\infty} + \frac{\left\|\vec{u}_d\right\|^2}{2} \right] \times U_\infty LWC_\infty \beta \\ &\quad - L_{evap}\dot{m}_{evap} + \dot{m}_{ice}\left[L_{fus} - C_{p,ice}T_{equi} \right] + h_c\left(T_{equi} - T_\infty\right) \\ &\quad + \sigma\varepsilon\left[T_{equi}^4 - T_\infty^{\,4} \right] + C_{p,w}T_c\left(U_\infty LWC_\infty\beta - \dot{m}_{evap} - \dot{m}_{ice}\right). \end{aligned} \tag{19}$$

In Eqs. (18) and (19), there are three unknowns to be computed: water film thickness (h_f), equilibrium temperature (T_{equi}), and mass of accreted ice ($\dot{m}_{ice}$). Here, ρ_w, μ_w, $C_{p,w}$, $C_{p,ice}$ are the density, dynamic viscosity, the specific heat of the water, and the specific heat of ice at constant pressure, respectively. Moreover, $U_\infty LWC_\infty\beta$ and $\dot{m}_{evap}$ stand for the instantaneous water droplet impingement mass and instantaneous evaporation mass, respectively. The latent heat of fusion and evaporation are represented by L_{fus} and L_{evap}. Free-stream air velocity, temperature, LWC, and the temperature of the water droplet are denoted by U_∞, T_∞, LWC_∞ and $\tilde{T}_{d,\infty}$, respectively. Average liquid film velocity ($\bar{u}_f$) which is a function of wall shear stress and convective heat transfer coefficient (h_c) are obtained from the air solver. On the other hand, the droplet impact velocity vector ($\vec{u}_d$) and collection efficiency (β) are transferred from the droplet solver. Since there are only two governing equations available, compatibility relations are necessary to close the system. The compatibility equations can be given as,

$$
\begin{aligned}
&h_f \geq 0, \\
&\dot{m}_{ice} \geq 0, \\
&h_f T_{equi} \geq h_f T_c, \\
&\dot{m}_{ice} T_{equi} \leq \dot{m}_{ice} T_c.
\end{aligned}
\tag{20}
$$

The above four compatibility equations can be represented into three for the three different regimes of ice accretion. The first regime corresponds to running water with no ice accretion, which is basically above the freezing point. Hence this regime can be described as $h_f \geq 0,\ T_{equi} \geq T_c = 0,$ where T_c is the critical temperature. The second regime corresponds to glaze ice growth which happens when the water film and ice are present simultaneously. The equilibrium temperature is assumed to be the freezing temperature of water; hence this regime can be expressed as $h_f \geq 0,\ T_{equi} = T_c,\ \dot{m}_{ice} \geq 0$. The final regime corresponds to rime ice cases, where the liquid film flows are not available and only dry ice accumulation is possible. This regime can be described as $h_f = 0,\ T_{equi} \leq T_c,\ \dot{m}_{ice} \geq 0$.

2.4. Ice-shape generation solver

The surface grid was moved in the perpendicular direction based on the ice thickness obtained using the thermodynamic module's ice mass information. By interpolating the ice thickness and normal vector at each surface to the node points, a newly formed surface resulting from ice accretion was produced.

3. Validation of computational models

3.1. Airflow module

(a) Airfoil

The aerodynamic solver was validated for flow over GLC305 [66] and verified over a NACA0012 [67] airfoil for the coefficient of pressure, and the convective heat transfer coefficient, respectively. In the experiment with the GLC305 airfoil, the free stream Mach number and Reynolds numbers were 0.23 and 4.9×10^6, respectively. In the validation study, the Spalart-Allmaras turbulence model was employed, which incorporated a fully turbulent boundary layer with a smooth wall. The pressure coefficient around the GLC305 airfoil under the given

metrological conditions was compared with the experimental results, as shown in Fig. 3. The pressure coefficient prediction along the airfoil surface was compared with the experimental results. There was an excellent match between the computation and the experimental results.

In an icing simulation, the heat transfer coefficient has a significant effect on the ice shape prediction. The heat transfer coefficient over the NACA0012 airfoil was compared with the LEWICE result. The freestream Mach and temperature were 0.32 and 262.04 K respectively. The heat transfer coefficient along the airfoil surface was computed and compared (Fig. 4) to LEWICE, revealing an adequate match.

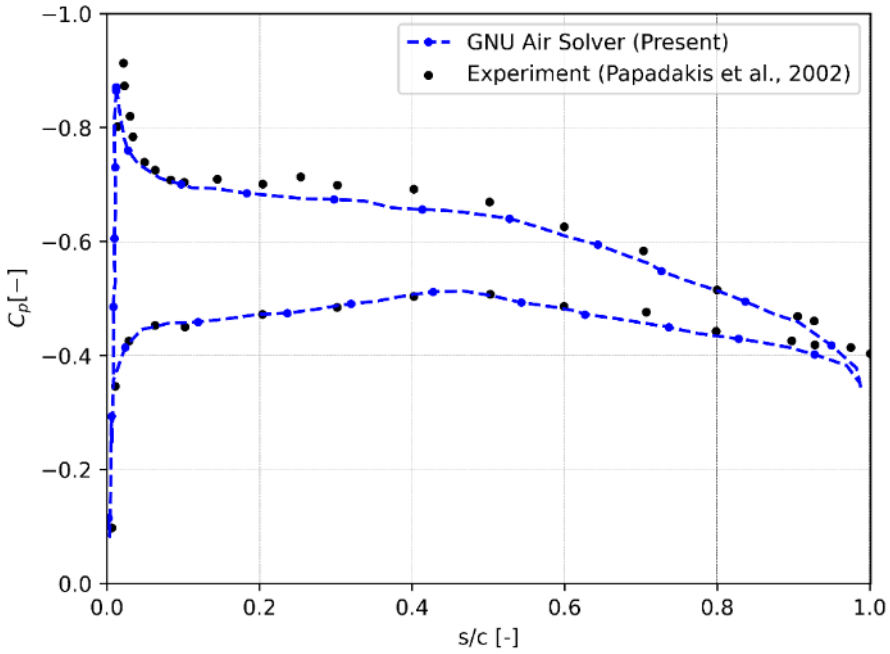

Fig. 3 Pressure coefficient (C_p) distribution around GLC305 airfoil (M = 0.23, Re = 4.9×10^6).

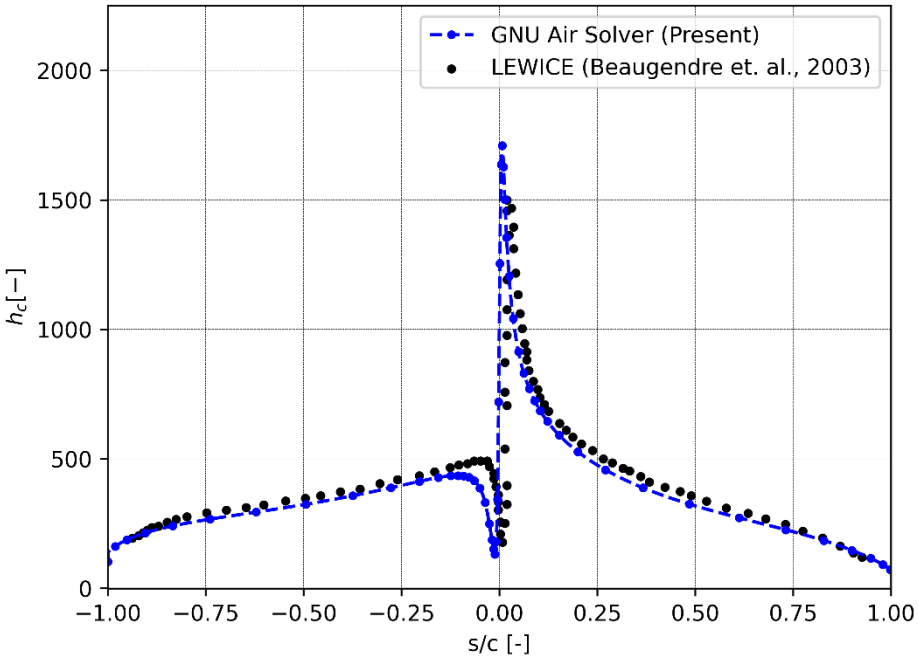

Fig. 4 Convective heat transfer coefficient (h_c) distribution around NACA0012 (M = 0.32, T_∞ = 262.04 K).

(b) Rotorcraft

The present method was also applied to the NASA ROBIN configuration [68], which is a combination of a generic helicopter fuselage and a four-bladed rectangular rotor system. The rotor consists of four NACA0012 airfoil blades with an -8° linear twist. The blade has a radius of 0.86 m and an aspect ratio of 12.98, respectively. The fuselage length (L) is 2 m, and the coordinates of the observation location are non-dimensionalized by the fuselage length. The rotor shaft has a tilt of 3° in the forward direction. The simulations were performed with the ROBIN configuration at an advance ratio and blade tip Mach number of 0.15 and 0.53, respectively, for two different rotor thrust coefficients of 0.008 and 0.0065. The time discretization for coupling was maintained at 4° throughout the simulation in both cases.

The NASA experiment measured the steady and unsteady pressures at a large number of points on the fuselage surface. For validation of the computational findings, the pressure coefficients at some selected points among the stated points, shown in Fig. 5, were compared with the computational results. The mesh independence study was carried out during the validation process and the same mesh was utilized for aerodynamic simulation of other cases. The pressure coefficient is defined by $C_P = (P - P_\infty)/(0.5\rho V_{tip}^2)$, and the unsteady pressure was obtained by

subtracting the time-averaged value from the pressure. The representative pressure distribution on the ROBIN fuselage and rotor wake interaction is shown in Fig. 6.

The primary effect of the rotor's rotation is to generate downwash—a flow of air pushed downwards as the rotor blades generate lift. This downwash can increase the local airspeed and dynamic pressure over points on the fuselage directly below the downwash flow path, potentially affecting the pressure coefficients measured at these points. Each blade tip generates a vortex as it slices through the air. These vortices trail behind the blade tips and move downwards and outwards. As they move past the fuselage, they can cause localized changes in pressure at the probe points. The effect is periodic and associated with the number of blades and their rotational speed. The interaction of the rotor wake with the fuselage creates complex airflow patterns that can affect the pressure distribution. This could cause changes in the pressure coefficients at the probes due to varying aerodynamic interference. Due to the forward flight condition (indicated by the advance ratio), the wake is not symmetrical. The advancing blade side will see a higher relative airflow, and the retreating side will see less. This asymmetry in the wake can cause differences in the pressures measured at the probes on either side of the centerline.

Probes D5, D6, D8, and D9 are positioned on the forward section of the fuselage, as depicted in Fig. 5. The predominant influence on these probes comes from the free stream airflow, which overshadows the effects of the rotor wake, leading to similar pressure coefficient characteristics at all these locations. The pressure coefficient oscillations are due to the influence of the rotor on the flowfield, with the amplitude of these oscillations being consistent across all four probes. This consistency in the oscillation pattern is attributed to the quad-bladed design of the rotor, with each cycle corresponding to one of the four blades passing by the measurement points.

The pressure fluctuations at probes D4, D19, D13, and D25 as shown in Fig. 5 are due to the rotor's counterclockwise rotation and its aerodynamic impacts on these specific fuselage points. For D4 and D19, located on the side of the fuselage, the primary effect is the lateral downwash caused by the rotor's rotation. This downwash leads to an increase in local airspeed and dynamic pressure at these side points, influencing their pressure coefficients. Additionally, the powerful tip vortices generated by each rotating blade, which extend outward and downward, intermittently

impact these probes. However, the similar and relatively low amplitude of pressure fluctuations at D4 and D19 is due to the downstream location of the rotor wake, shielding the strongest part of the vortex, resulting in less pronounced variations.

In contrast, probes D13 and D25 will exhibit a different pattern of pressure fluctuations, with D13 showing higher amplitude variations than D4 and D19, and D25 exhibiting the highest amplitude. This escalation in amplitude can be attributed to the asymmetric effect of the rotor wake, intensified by the advance ratio of the aircraft. In forward flight, the advancing side of the rotor, which moves into the relative wind, generates different flow characteristics compared to the retreating side, leading to asymmetrical wake effects. D13 and D25, located on the advancing side of the rotor, are subjected to these varied flow conditions, including higher relative velocity over the rotor blades. This results in more pronounced pressure variations at these points, with D25, possibly being in a position that experiences the most direct and intense interaction with the wake, thus showing the greatest amplitude in pressure fluctuations.

The hub region is often characterized by a complex flow structure due to the presence of the hub vortex, which is a large-scale vortex structure that is generated by the rotating blades near the rotor hub. This hub vortex can have a significant impact on the local flow field. However, the hub vortex tends to be more stable and less energetic compared to the tip vortices, which could result in lower pressure variation amplitudes at D17. The tip vortices are stronger and contain more energy than the hub vortex. As these vortices are shed from the blade tips, they convect downstream and can interact with the tail region, where D14 is located. This interaction can induce higher amplitude pressure fluctuations at D14 due to the more energetic nature of the tip vortices.

Case 1: The hybrid NVLM VPM/CFD solver was utilized to examine its performance in the ROBIN flow field, as described in Table 2. The first case (Case 1) was chosen to have a rotor thrust coefficient of 0.008, also detailed in Table 3. The variation in unsteady pressure for the nose regions (D5, D6, D8, and D9) are presented in Fig. 7 (a), 7 (b), 7 (c), and 7 (d), respectively.

The results of the present solver were compared with Bae *et al*. [22]. In some cases, except at D8, a small amount of phase shift was observed. The pressure peaks were slightly under-predicted in all cases, although for D9, the present simulation results matched the experiment, and even the

amplitude was observed to be similar. The probes D13 and D25 on the advancing side of the fuselage were compared. The predicted amplitude above the mean was similar to those of other computational results, but the present solver could not properly predict the lower amplitude below the mean for probe D13, while for probe D25, an excellent match with Bae *et al*. [22] was observed. The pressure coefficient variation on the fairing portion at D17 matched the other computational results well and with the experiment in the overall sense with the correct phase. For the unsteady pressure coefficient on the retreating side for probe locations D4 and D19, an excellent match with the experiment was observed. For the probe location at the tail boom, D14, the pressure coefficient prediction matched the other computational results well, and the correct phase prediction was also observed.

Table 2 Model description of ROBIN

Parameter	Value
Number of blades, NB [-]	4
Aspect ratio, AR [-]	12.98
Rotor radius, R [m]	0.86
Advance ratio, μ [-]	0.15
Angular velocity, Ω [RPM]	1995
Twist angle, θ_{twist} [deg.]	-8
Tilt angle, θ_{tilt} [deg.]	-3
Blade sectional profile	NACA 0012 airfoil

Table 3 Flow description of ROBIN for Case 1

Parameter	Value
Target thrust coefficient, C_T [-]	0.008
Collective pitch angle, θ [deg.]	12.0
Longitudinal cyclic pitch, A1 [deg.]	-2.9
Lateral cyclic pitch, B1 [deg.]	2.5

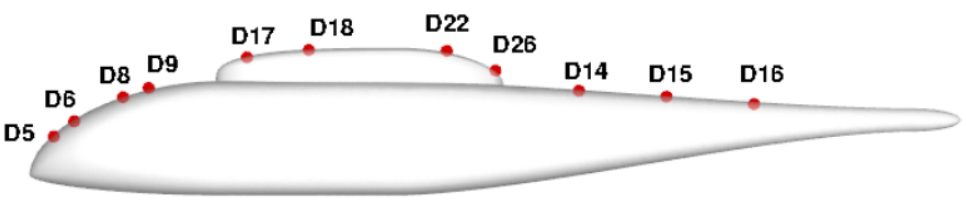

(a) Fuselage Center-line

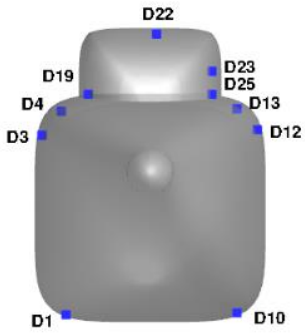

(b) Fuselage Ring, $X/L = 0.4475$

Fig. 5 Probe locations for unsteady pressure on ROBIN fuselage.

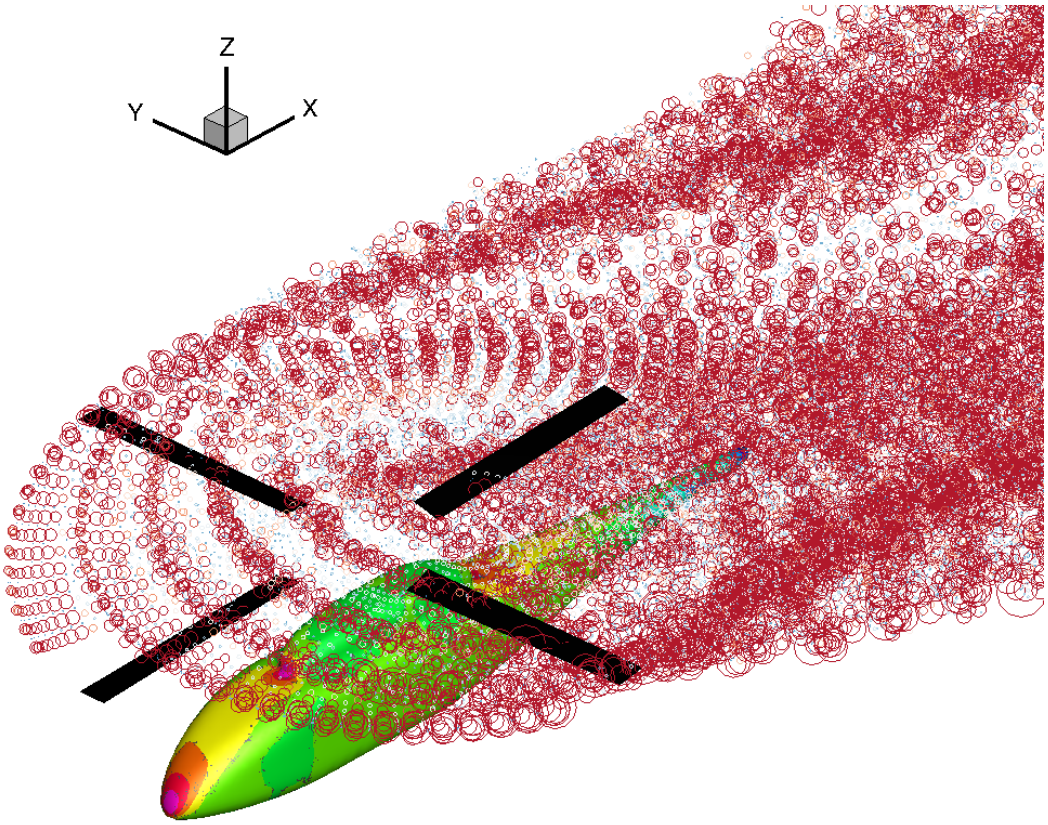

Fig. 6 Wake structure around ROBIN fuselage along with surface pressure distribution.

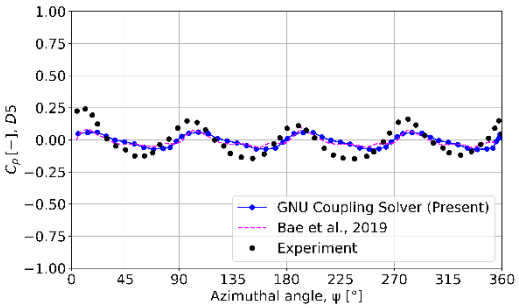

(a) C_p comparison at location D5.

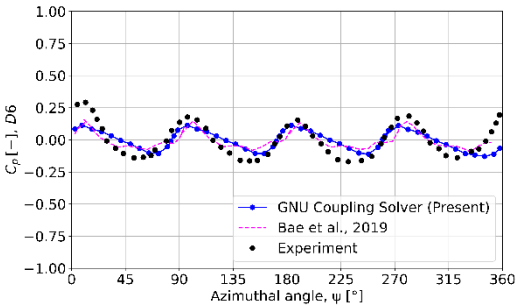

(b) C_p comparison at location D6.

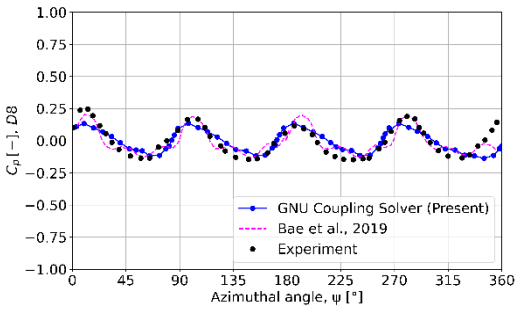

(c) C_p comparison at location D8.

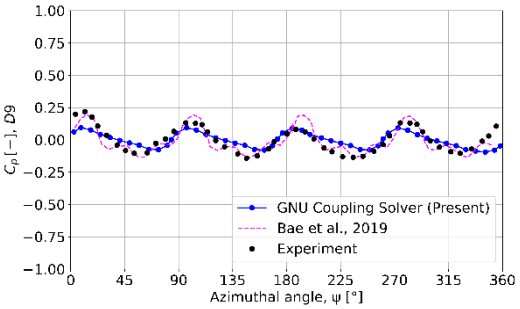

(d) C_p comparison at location D9.

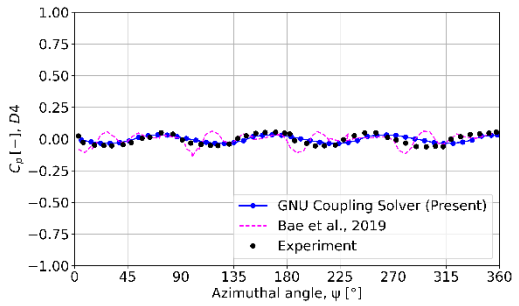

(e) C_p comparison at location D4.

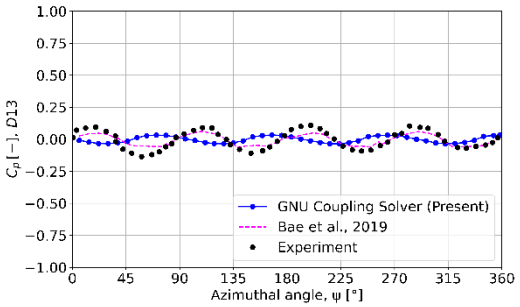

(f) C_p comparison at location D13.

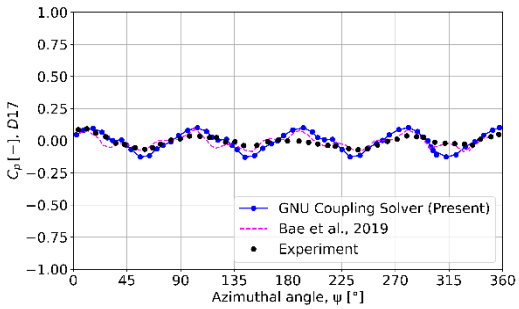

(g) C_p comparison at location D17.

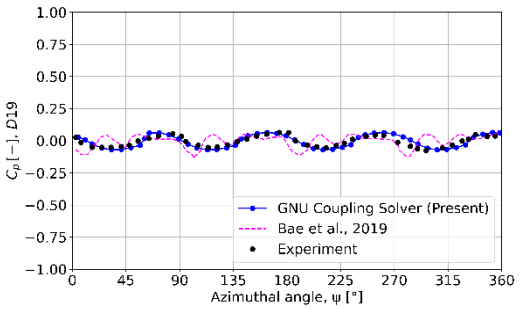

(h) C_p comparison at location D19.

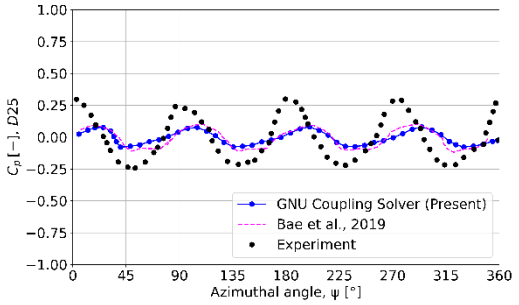

(i) C_p comparison at location D25.

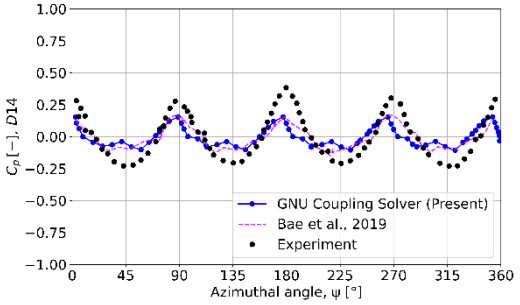

(j) C_p comparison at location D14.

Fig. 7 Pressure coefficient (C_p) comparison at location (a) D5, (b) D6, (c) D8, (d) D9, (e) D4, (f) D13, (g) D17, (h) D19, (i) D25, (j) D14.

Table 4 Flow description of ROBIN for Case 2

Parameter	Value
Target thrust coefficient, C_T [-]	0.0065
Collective pitch angle, θ [deg.]	10.3
Longitudinal cyclic pitch, A1 [deg.]	-2.7
Lateral cyclic pitch, B1 [deg.]	2.4

Case 2: The hybrid NVLM VPM/CFD solver was utilized to examine its performance on the ROBIN flow field. The second case (Case 2) was chosen to have a rotor thrust coefficient of 0.0065, also detailed in Table 4, and the validations are provided in Fig. 8. The computational results of the present aerodynamic solver showed good agreement with the experiment and are shown here for some selected probe locations. The probe locations D5, D6, and D15 were compared with coupling code (VLM+VPM+Panel) by Jang *et al*. [69], VTM by Kenyon *et al*. [70], and Euler code with an overset mesh by Lee *et al*. [71]. The present method predicted the pressure coefficient with adequate accuracy.

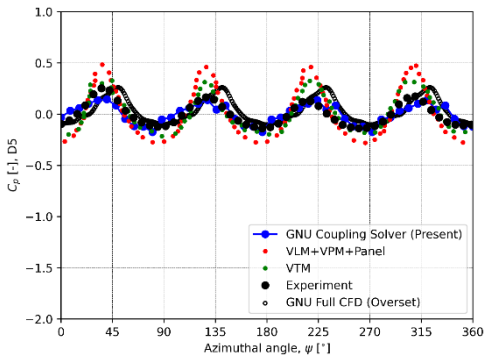

(a) C_p comparison at location D5.

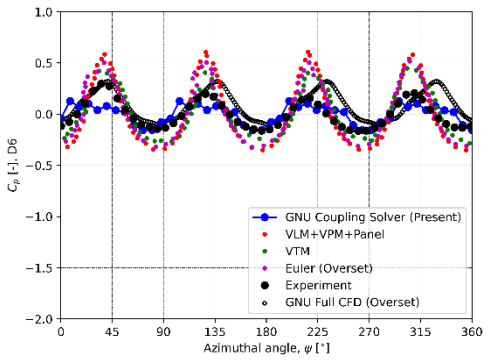

(b) C_p comparison at location D6.

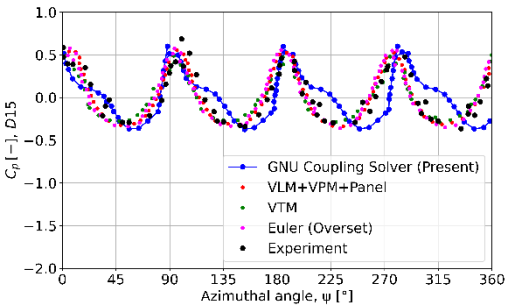

(c) C_p comparison at location D15.

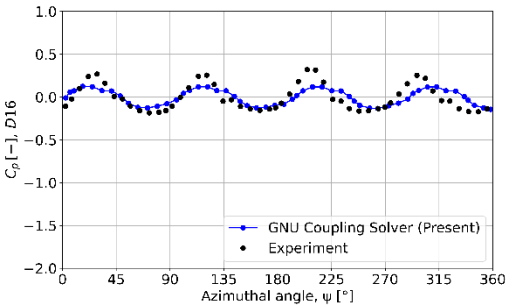

(d) C_p comparison at location D16.

Fig. 8 Pressure coefficient (C_p) comparison at location (a) D5, (b) D6, (c) D15, (d) D16.

We have compared our findings with various approaches previously documented in the literature. The high-fidelity technique employed by Lee et al. [71] involved the use of an overset method with an adaptive grid to analyze the rotor blade, applying the Euler equation (inviscid flow). This method was successful in capturing the pressure fluctuations at probe D15, as shown in Fig. 8. D15 is located in the tail region of the fuselage, an area significantly influenced by rotor wake due to downwash and interactions between the wake and the fuselage. In this region, the impact of viscosity is relatively minor. Similarly, the approaches used by Jang et al. [69] and Kenyon et al. [70] showed comparable trends. On the other hand, probes D5 and D6, positioned at the front of the fuselage, are predominantly influenced by the free stream flow rather than the rotor wake. In these locations, characterized by lower Reynolds numbers, the effects of viscosity are more noticeable. Our current method accounts for the influence of viscosity and, as a result, provides a more accurate prediction than the other methods reviewed. Moreover, the present method uses NVLM for blade modeling which takes into account the non-linear effects and improves the predictions as shown in Fig. 7 (d), 7 (e), and 7 (h).

Table 5 Comparison of CPU time (52 Intel processors of 2.4 GHz; 10 revolutions)

Cases / Methods	Overset mesh (STAR-CCM+)	Hybrid (GNU)
Airflow computation	133 hrs.	15.65 hrs.
Droplet computation	16.9 hrs.	2.0 hrs.
Rotorcraft advance ratios (4 cases)	(133+16.9)×4= 599.6 hrs.	(15.65+2.0)×4=70.6 hrs.

Rotor thrust coefficients (3 cases)	(133+16.9)×12=1,798.8 hrs.	(15.65+2.0)×12=211.8 hrs.
Icing conditions (30 cases in Appendix C)	(133+16.9)×360=53,964 hrs.	(15.65+2.0)×360=6,354 hrs.
Total computing time	53,964 hrs. = 6.25 yrs.	6,354 hrs. = 0.735 yrs.

We have also simulated Case 2, employing the same convective flux scheme, time discretization scheme, and identical spatial-temporal order of accuracy across the same surface mesh using CFD overset methodology (Simcenter STAR-CCM+ [71]). We have compared the pressure coefficient at D5 and D6 as shown in Fig. 8, which is marked with GNU (Overset). The predicted pressure coefficients are in close agreement with the experiment. The prediction at probe D6 when compared with Euler code with an overset mesh by Lee et al. [72], clearly indicates the improvement in accuracy when viscous flux with turbulence was considered.

In our in-house hybrid solver, the rotor blade advances by 3° for each time step, and it takes 15.65 hours of CPU time for 10 revolutions using 52 Intel processors of 2.4 GHz each, whereas CPU time in full CFD simulation based on an overset mesh for same number of revolutions was 133 hours, making the hybrid solver approximately 8.5 times faster than the full CFD solver, as summarized in Table 5. Considering the multiple rotorcraft advance ratios, rotor thrust coefficients, and icing conditions required in a typical ice certification simulation, the current results show very high computing time savings of 0.725 years vs. 6.16 years for 52 Intel processors.

3.2. Droplet module

The droplet solver was validated using an experimental case performed by NASA IRT [66] on a GLC305 airfoil. The unstructured mesh with approximately a hundred thousand cells was used to perform the simulation. The free stream Mach and Reynolds numbers were 0.23 and 4.9×10^6, respectively. The liquid water content (LWC) and median volumetric diameter (MVD) of the droplets were 0.05 g/m^3 and 21.0 μm with non-SLD and mono-dispersed distribution in space.

The collection efficiency here is defined as $\beta = LWC\,\boldsymbol{U}\cdot\boldsymbol{n}/LWC_\infty U_\infty$. The collection efficiency along the surface of the airfoil was compared with the experiment [66]. The droplet model

accurately predicted the magnitude and location of maximum collection efficiency, as shown in Fig. 9. However, the impingement limit was under-predicted by the present model. This could be because in the experiment, creating mono-dispersed droplets is difficult and is dependent on the precision of the spraying nozzle. Therefore, there is always a chance that there were deviations from the mono-dispersion assumed in the experimental setup. The poly-dispersed droplet distribution has a large impingement limit [73].

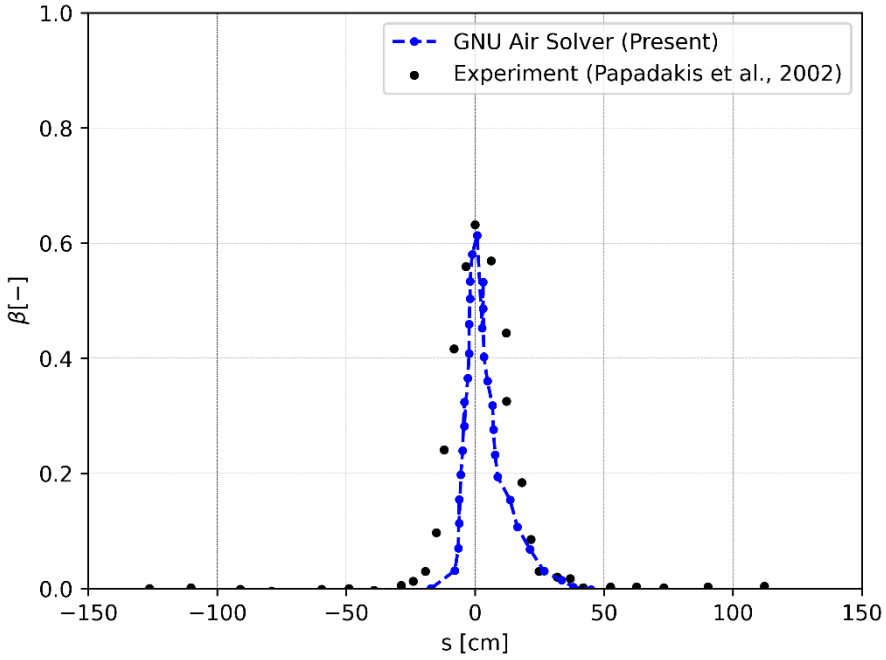

Fig. 9 Collection efficiency (β) around GLC305 airfoil (M = 0.23, Re = 4.9×10^6, LWC = 0.05 g/m^3, and MVD = 21 µm).

3.3. Ice accretion module

Ice accretion during flight is a complex process, the details of which depend on the atmospheric and flight conditions. There are a few experimental studies [74] to investigate the transient ice accretion process under various icing conditions, but the focus is placed on the final ice shapes formed after exposure for a set duration to icing conditions.

In this study, the 3D ice accretion solver was validated using an experimental case studied by NASA IRT, on a GLC-305 swept wing [74]. After the successful prediction of the airflow field and droplet distribution around the wing, the results were used as the input for the ice accretion solver. The metrological condition used for the current validation is shown in Table 6 as follows:

Table 6 Metrological conditions for GLC-305 wing ice validation

Parameter	Value
Temperature [K]	269
Pressure [KPa]	100
Velocity [m/s]	111.25
AoA [deg.]	4
MVD [μm]	20
LWC [g/m^3]	0.68
Mach [-]	0.24
Lateral cyclic pitch, B1 [deg.]	2.4

The computed results were compared with the experimental results from three sections of the wing geometry. The first section was at the root, the second at the 25-inch span from the root, and the final section was at the 50-inch span from the root. Pictorial views of the sections and the ice accretion comparison at the root, 25-inch, and 50-inch sections are shown in Fig. 10.

The current numerical method slightly overestimated the ice shape on the upper surface of the wing at the root section. On the other hand, it accurately predicted the ice shape at the 25-inch section. However, there were small discrepancies observed in the 50-inch section. However, the overall ice prediction on the wing was satisfactory in comparison with the experiment [74] and other computations [75].

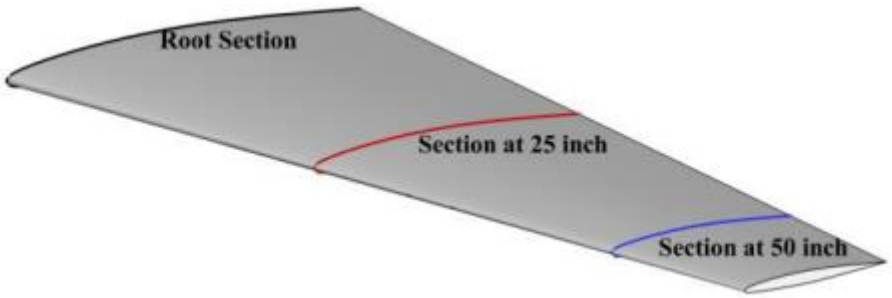

(a) GLC-305 wing cut sections.

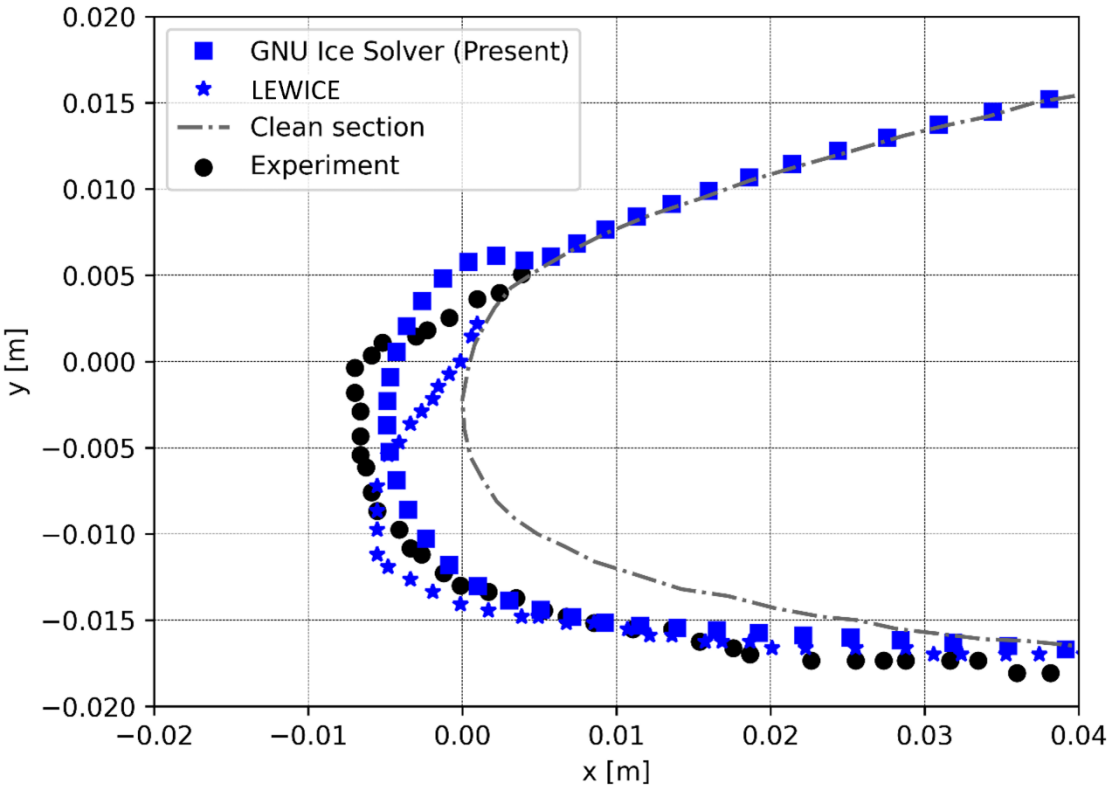

(b) GLC-305 ice shape validation at root cut sections.

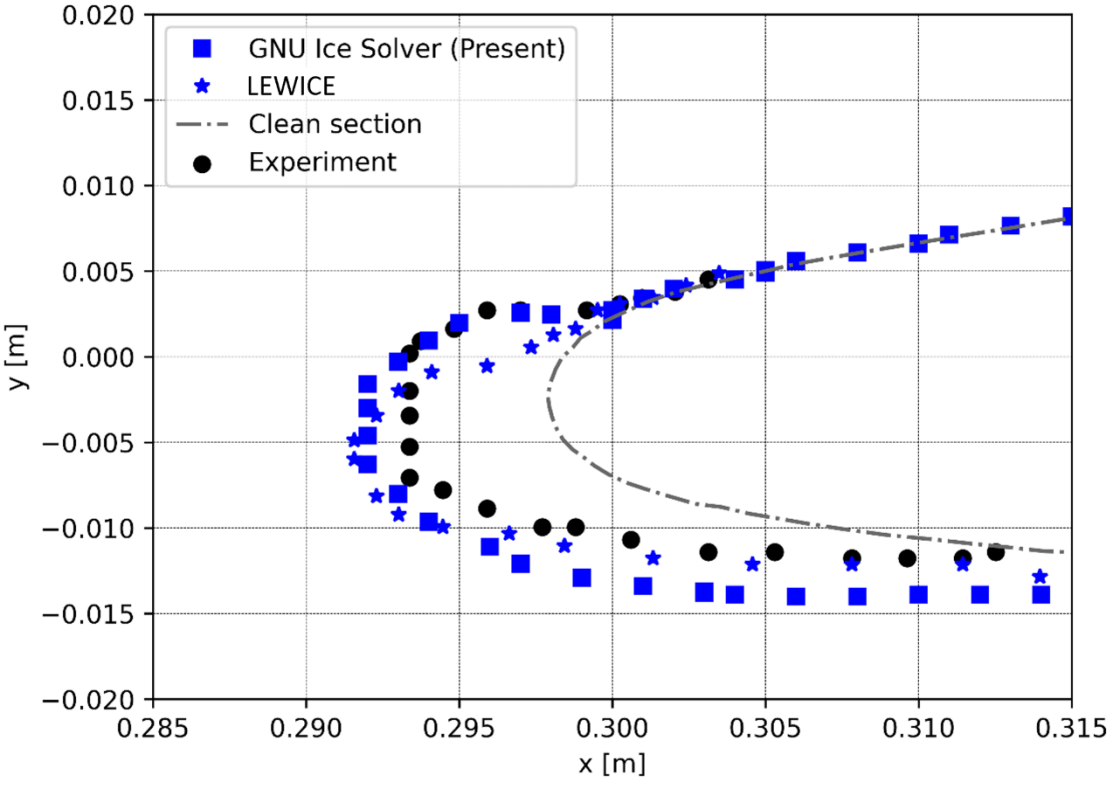

(c) GLC-305 ice shape validation at 25 inches cut sections.

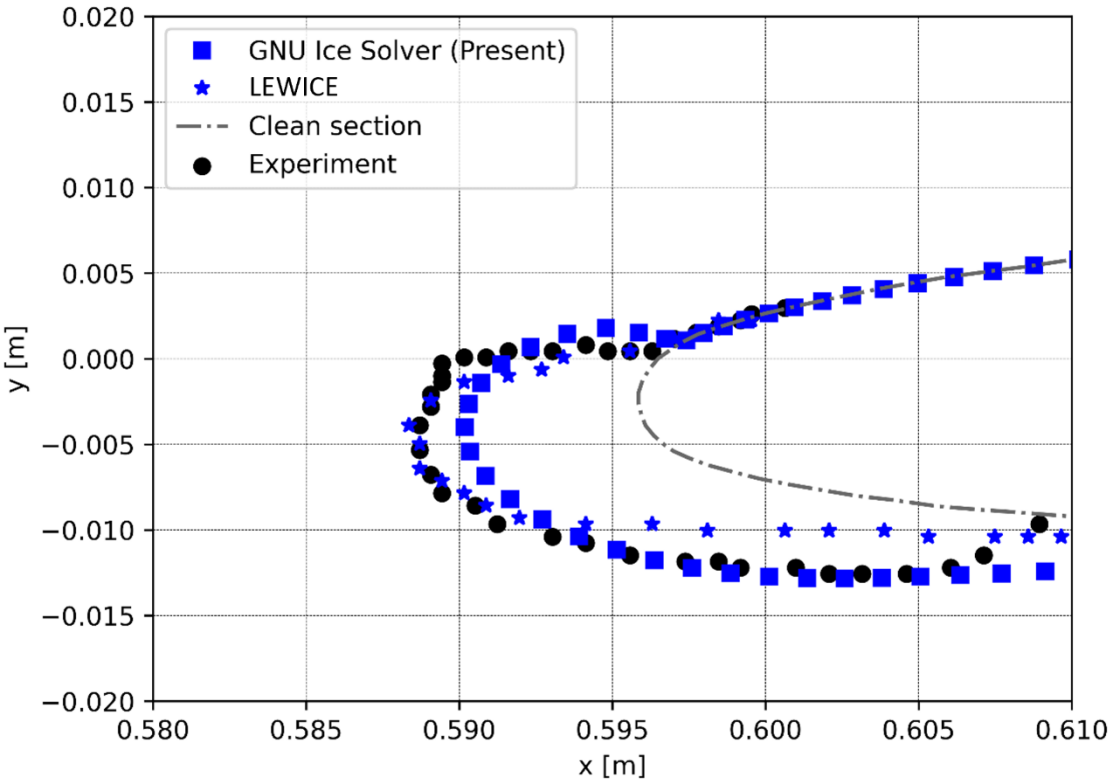

(d) GLC-305 ice shape validation at 50 inches cut sections.

Fig. 10 GLC-305 wing and validation of ice shapes at three different sections.

4. Results and discussion

The effect of advance ratio and rotor thrust coefficient on the location and mass of ice accretion on the rotorcraft fuselage was studied. Four modules, namely aerodynamic, droplet, ice accretion, and ice-shape generation, were utilized to predict ice accretion on the fuselage.

4.1. Effect of advance ratio

(a) Aerodynamic results

A visualization of the flow structure for different advance ratios (μ=0.051, 0.151, 0.232 as summarized in Table 7) at constant target rotor thrust coefficient (C_T =0.008) was performed using Q-criterion. Q-criterion as described by Dubief and Delcayre [76]:

$$Q = \frac{1}{2}\left(\Omega_{ij}\Omega_{ij} - S_{ij}S_{ij}\right) \tag{21}$$

The areas where Q > 0 indicate that the rotation rate $\Omega^2 = \Omega_{ij}\Omega_{ij}$ was higher than the strain rate $S^2 = S_{ij}S_{ij}$. Here, $\Omega_{ij} = (u_{i,j} - u_{j,i})/2$ and $S_{ij} = (u_{i,j} + u_{j,i})/2$ are the anti-symmetric and symmetric

components of $\nabla\mathbf{u}$. Figure 11 illustrates the computation domain for both the Eulerian (CFD grid) and the Lagrangian (particles) framework to solve the flow field around the rotorcraft. Figure 12 shows the iso-surface at Q=1000 when the four blades were at azimuth angles of 0°, 90°, 180°, and 270°, respectively. The bottom figure illustrates the same quantity at the mid-plane of the fuselage. At the lowest advance ratio, the maximum amount of interaction of wake and fuselage frontal and tail boom was noticed, leading to a high value of wake skew angle. In contrast, at the highest advance ratio, due to the high convection, the wakes were convected downstream. The least amount of interaction was observed with a low value of wake skew angle. The aerodynamic flow fields were initialized in the droplet solver to calculate source terms in the droplet governing equation.

Table 7 Conditions for icing with a fixed rotor thrust coefficient

Parameter	Value
Advance ratio, μ [-]	0.051, 0.151, 0.232
Thrust coefficient, C_T [-]	0.008
Free stream temperature, T_∞ [K]	258.15
Liquid water content, LWC [g/m^3]	0.4
Median volumetric diameter, MVD [μm]	18.6
Icing time, T_{ice} [minutes]	30.0

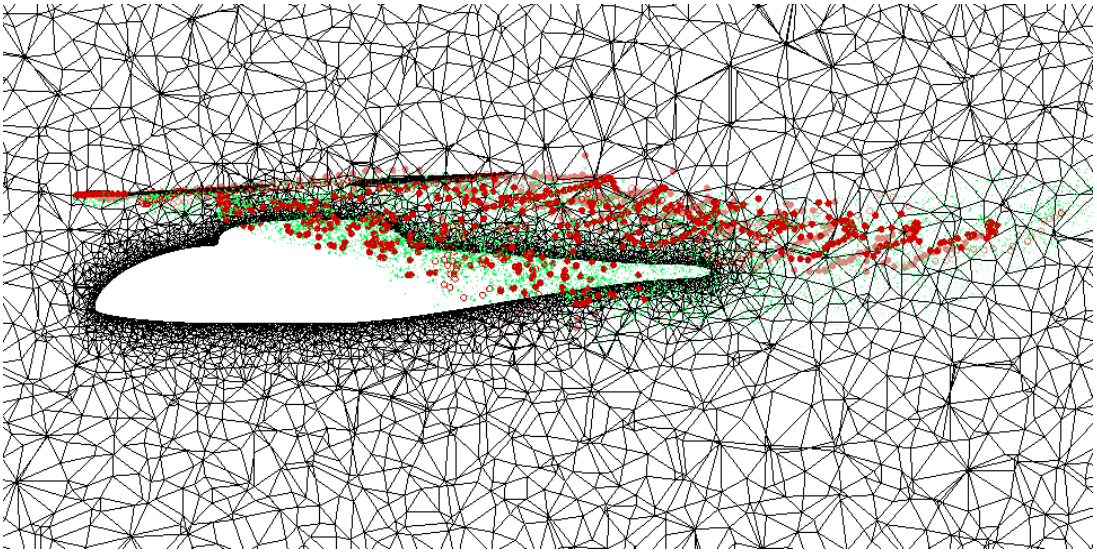

Fig. 11 Coupling algorithm using CFD grid and NVLM/VPM with VPM, where the wake particles originating from VPM and the flow field are solved using CFD mesh.

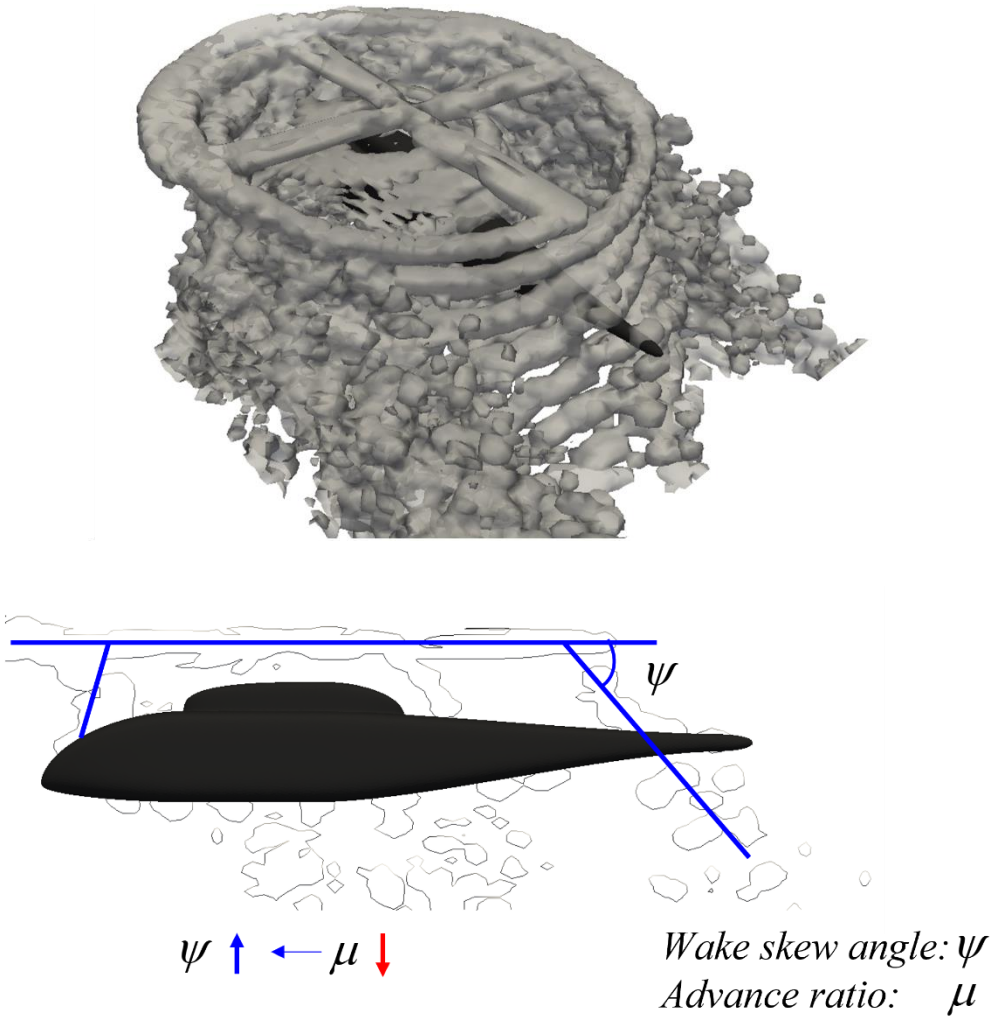

(a) $\mu = 0.051$.

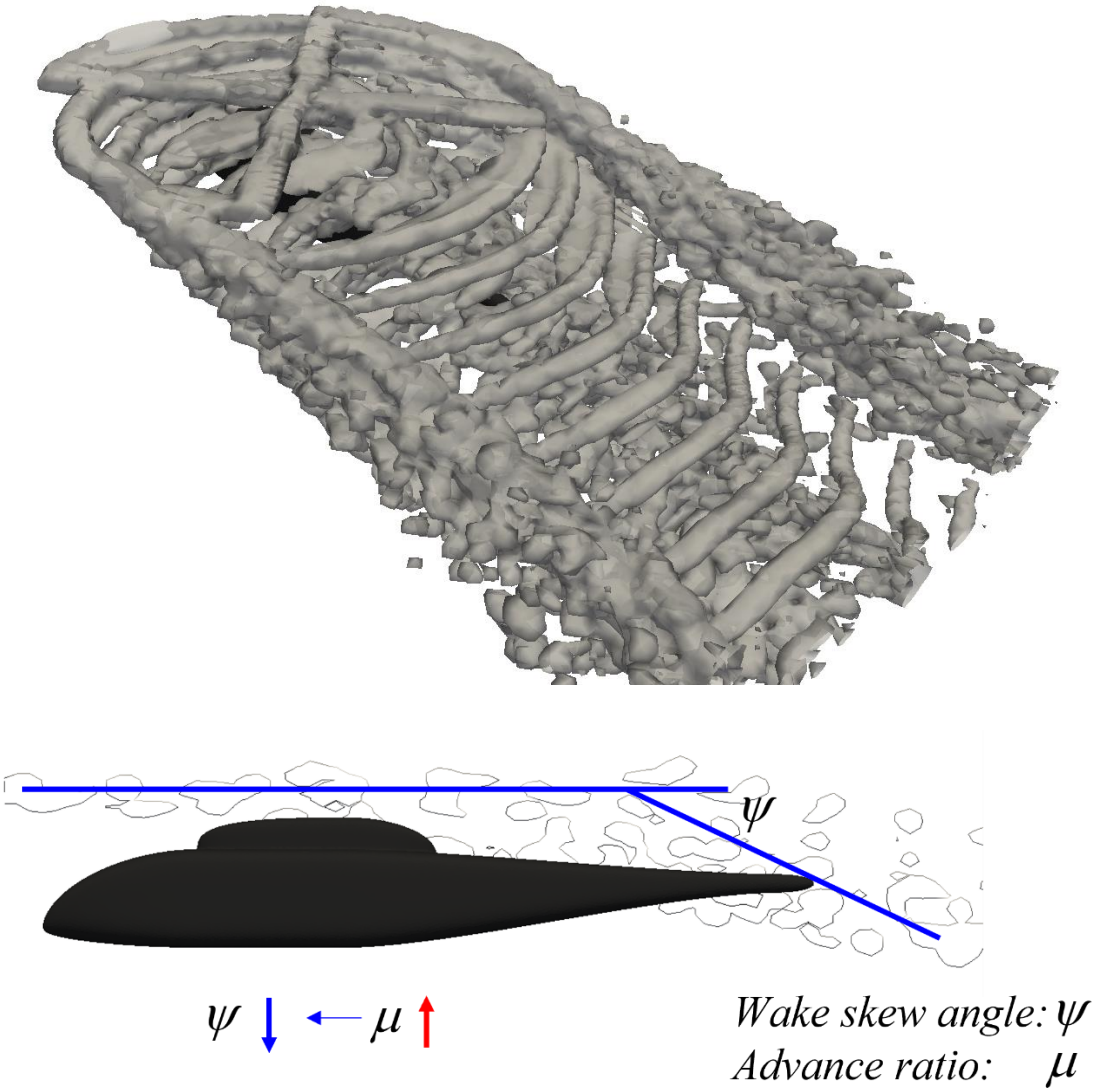

(b) $\mu = 0.151$.

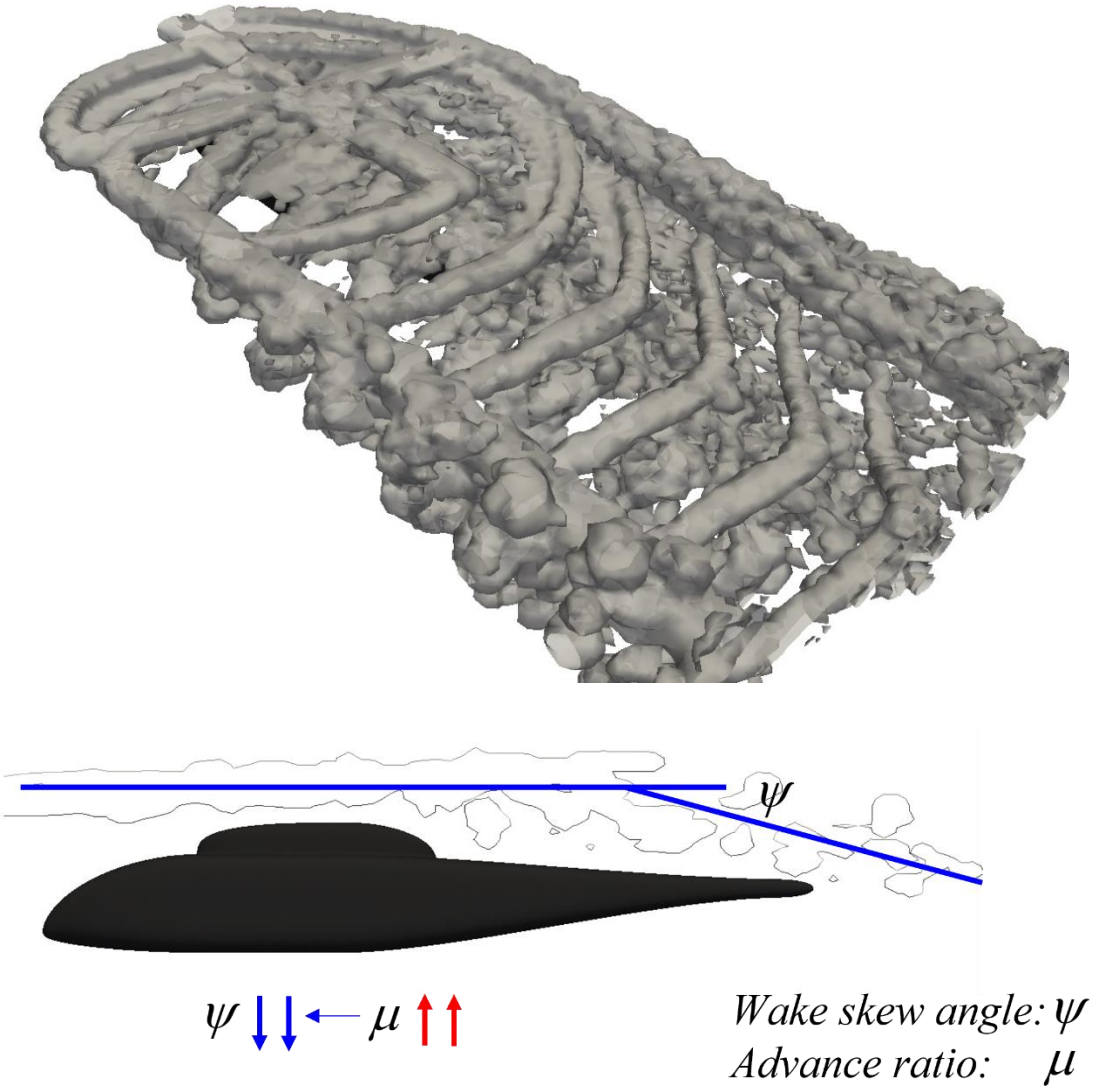

(c) μ = 0.232.

Fig. 12 The iso-surface at Q=1000 for different advance ratios ((a) μ = 0.051, (b) μ = 0.151, and (c) μ = 0.232)) with constant target thrust coefficient (C_T = 0.008).

(b) Droplet results

The aerodynamic results were averaged over one revolution and were utilized for the initialization in the droplet solver. The representative interaction of droplet trajectory with rotor wake and fuselage for the high advance ratio is shown in Fig. 13, where blue stream traces indicate the droplet trajectory and the rotor wakes are represented by green Q-criterion. The collection efficiency distribution at different advance ratios can be observed in Fig. 14. At a lower advance ratio, the highest amount of droplet deposition was observed in the frontal region of the fuselage and at the tail boom, as seen in Fig. 14 (a). This is evident from the wake interaction pattern, shown

in Fig. 12 (a). The large volume of fluid penetrates through the rotor plane and interacts with the frontal and tail boom of the fuselage. The volume of air is the carrier of the droplet stream and is deposited on the fuselage in the locations mentioned. For the highest advance ratio, illustrated in Fig. 14 (c), the highest amount of deposition was observed at the nose and engine intake, with very low deposition at the tail boom. The wake fuselage interaction at the highest advance ratio, shown in Fig. 12 (c), was negligible in the frontal region and low at the tail boom. Therefore, the highest deposition at the nose and engine intake is the result of the high free stream velocity, and the droplets were deposited at and near the stagnation region. Due to the very low interaction between the wake and low tail boom, only a small amount of deposition was observed in that region.

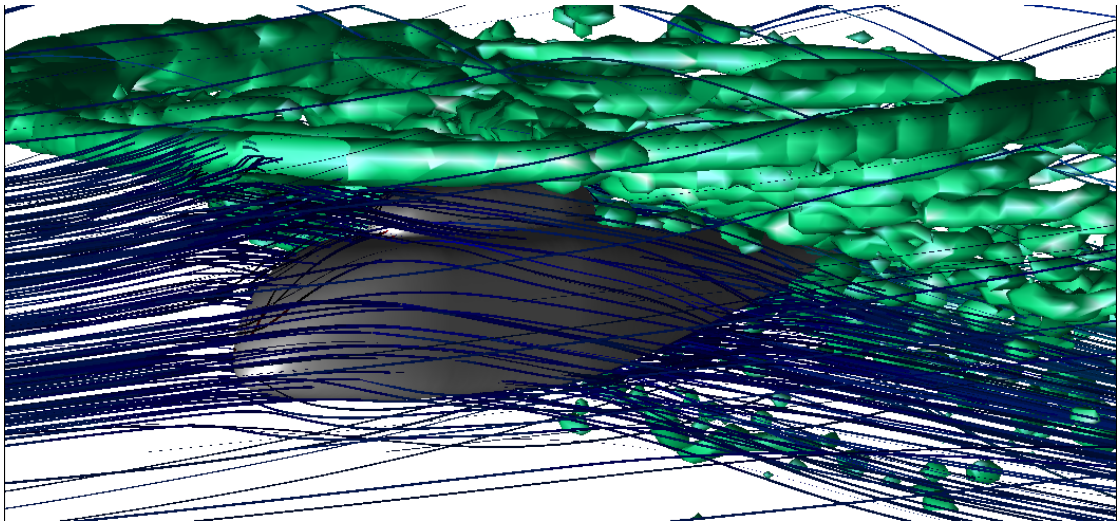

Fig. 13 Representative figure showing droplet particle trajectory and Q-criterion at high advance ratio.

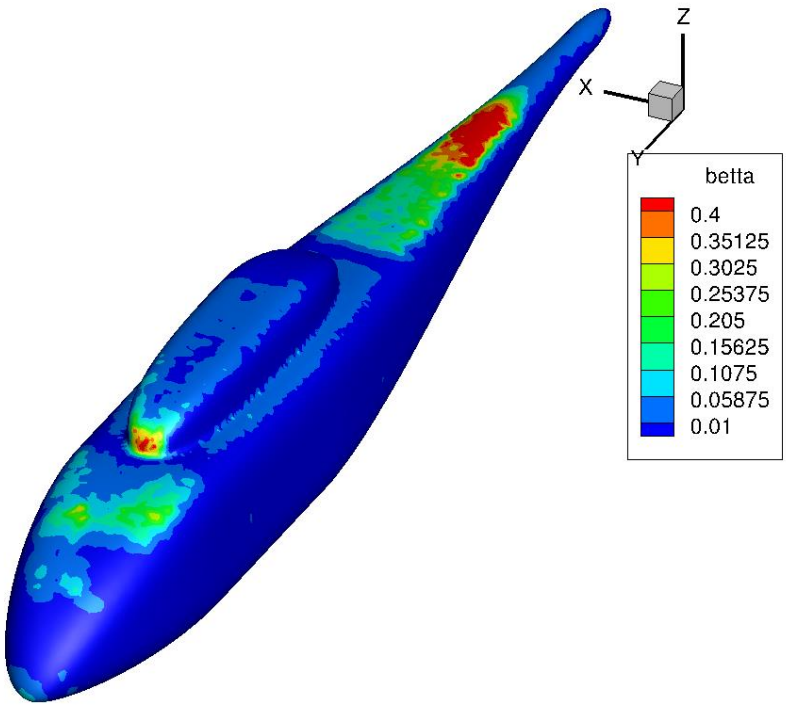

(a) $\mu = 0.051$.

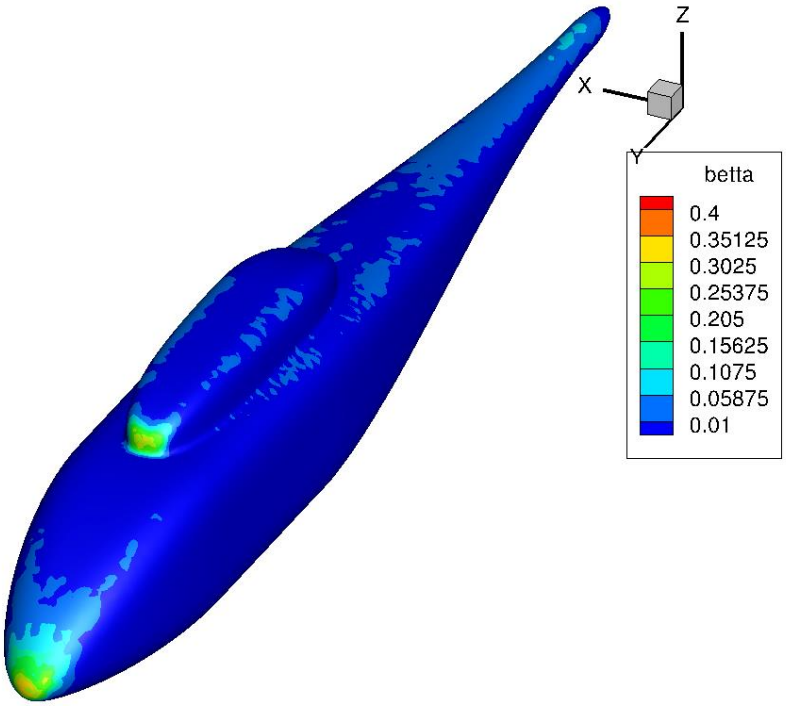

(b) $\mu = 0.151$.

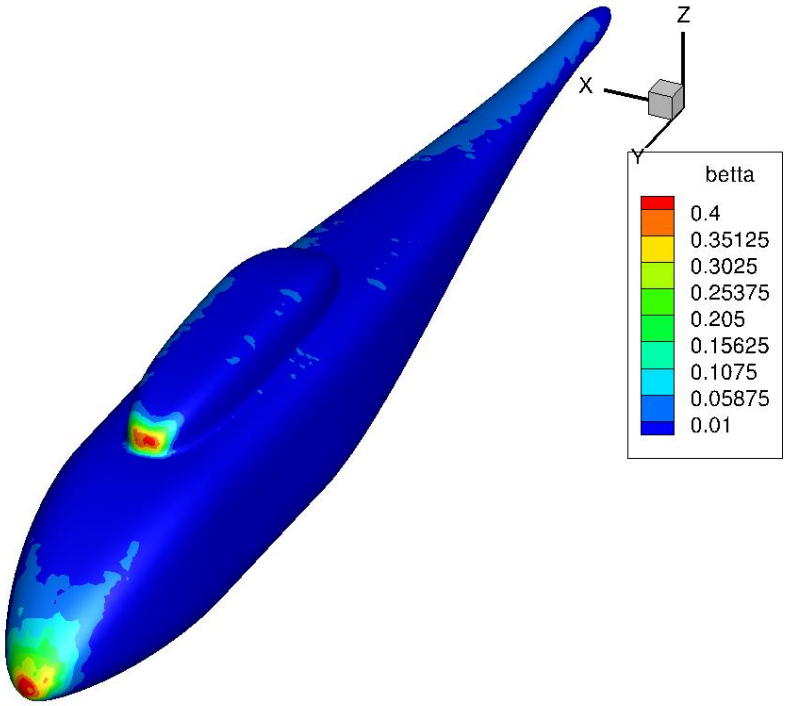

(c) $\mu = 0.232$.

Fig. 14 Collection efficiency for different advance ratios ((a) $\mu = 0.051$, (b) $\mu = 0.151$, and (c) $\mu = 0.232$)) with constant target thrust coefficient ($C_T = 0.008$).

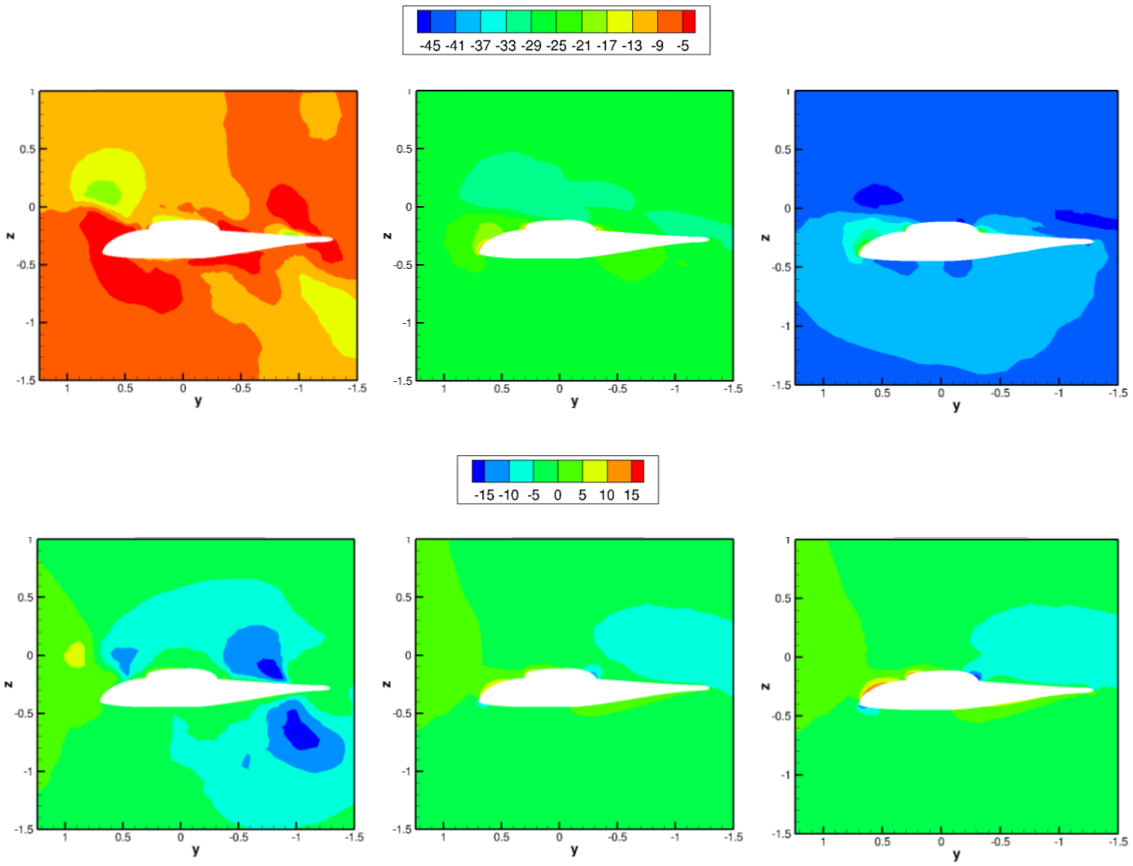

(a) $\mu = 0.051$. (b) $\mu = 0.151$. (c) $\mu = 0.232$.

Fig. 15 The droplet velocity field (top: streamwise velocity, bottom: down-wash velocity) at different advance ratios (μ = 0.051, 0.151, and 0.232, respectively).

The droplet phase average velocity distribution shown in Fig. 15 is also useful for understanding the pattern of collection efficiency, as illustrated in Fig. 14. At the lowest advance ratio, the fluid is pushed towards the fuselage, as evident from Fig. 15 (a) (bottom). The high impact velocity of the droplets on the fuselage in the downwash direction is responsible for the high deposition at the front and tail boom of the fuselage ($\boldsymbol{U}_{drop} \cdot \boldsymbol{n} > 0$). In contrast, for the highest advance ratio, the stream-wise component is the dominant component of velocity that carries the droplets and causes the deposition, as can be seen in Fig. 15 (c) (top). Since the stream-wise velocity is responsible for the deposition, maximum deposition occurs at and around the stagnation regions ($\boldsymbol{U}_{drop} \cdot \boldsymbol{n} > 0$), which are at the nose and engine intake, as shown in Fig. 14 (c). The effect in the mid-advance ratio is a combination of the above-mentioned phenomena.

(c) Ice accretion results

When the advance ratio or the forward speed increases, the rotor wake is inclined backward due to high wake convection, as can be seen in Fig. 12 for a given rotor thrust coefficient. Accordingly, the fuselage is less exposed to the wake effect. Hence, the advance ratio is a crucial parameter that determines the rotor wake and fuselage interaction. The effect of the advance ratio on the amount and location of ice accretion on the fuselage was studied, and three advance ratios (0.051, 0.151, and 0.232) were considered for identical rotor thrust coefficient and meteorological conditions, as given in Table 7.

With a low advance ratio, the tip vortex collides with the tail boom and frontal region of the fuselage due to low convection velocity. As shown in Fig. 15 (a), the downstream component of the velocity is highest near the frontal area and tail boom. The droplet carried by air through the rotor plane accelerates and impinges on the fuselage and causes icing near the frontal region, engine intake, and tail boom, as illustrated in Fig. 16 (a). The velocity vector of the droplet is perpendicular to the normal outward vector of the fuselage surface on the fuselage nose region. The droplets dodge the fuselage nose without collision. Therefore, more ice accretion occurs at the tail boom compared to the nose section. Fig. 17 (a) and 17 (b) show total ice mass accretion

and ice height at the fuselage center line for the longitudinal direction. As explained, both the ice mass and ice height at the tail boom region were observed to be higher. As the rotor rotates counterclockwise, the front of the engine intake has asymmetric ice accretion.

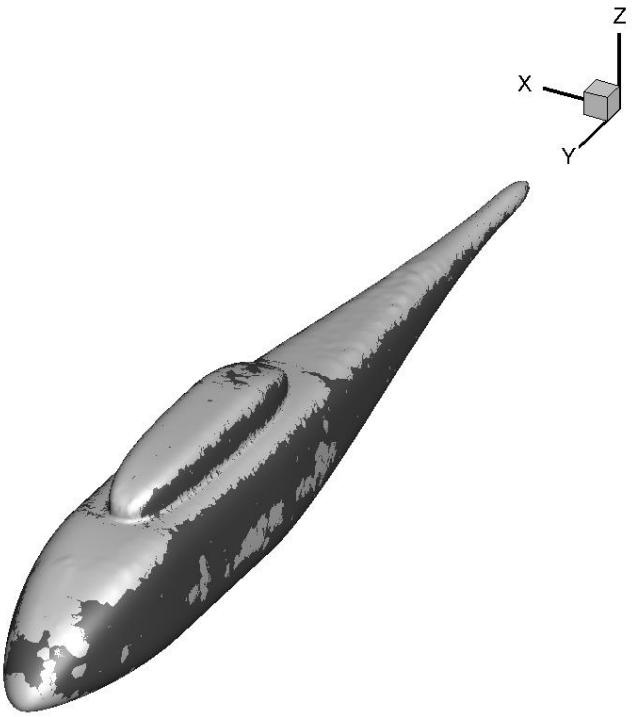

(a) $\mu = 0.051$.

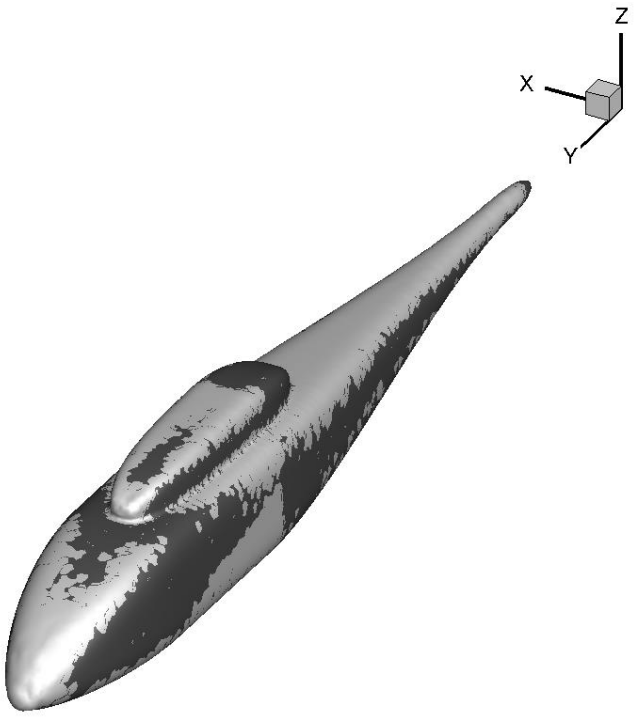

(b) $\mu = 0.151$.

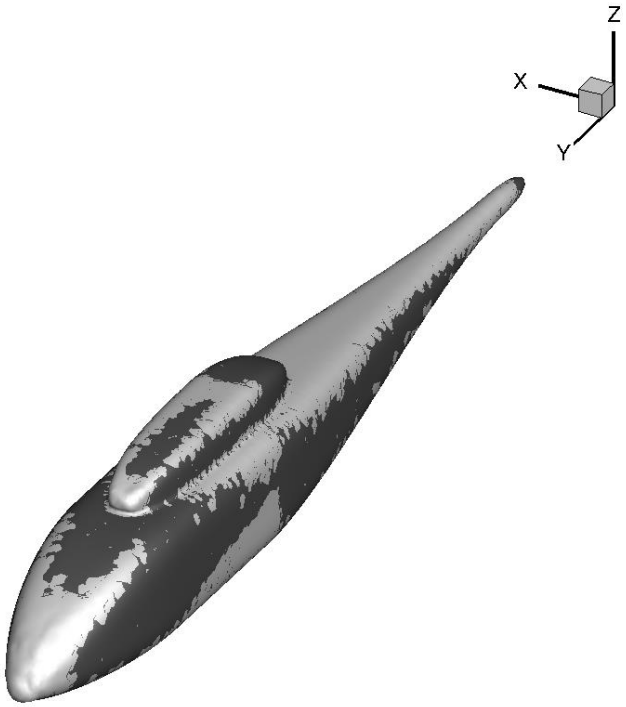

(c) μ = 0.232.

Fig. 16 Ice accretion location for different advance ratios ((a) μ = 0.051, (b) μ = 0.151, and (c) μ = 0.232)) with constant target thrust coefficient (C_T = 0.008).

At a high advance ratio, the rotor wake is moved downstream due to large convection velocity, as shown in Fig. 12 (c), without colliding with the tail boom. Due to the high forward speed, ice accretion occurs in the front of the fuselage, as is clearly shown in Fig. 17 (a). The large mass of droplets is delivered by the stream-wise component of the free stream flow, as shown in Fig. 15 (c), which causes a large deposition of droplets on the nose, as shown by the collection efficiency distribution in Fig. 14 (c). Therefore, a large amount of ice accretion was observed on the nose and engine intake, and there was very little ice accretion on the tail boom (Fig. 17).

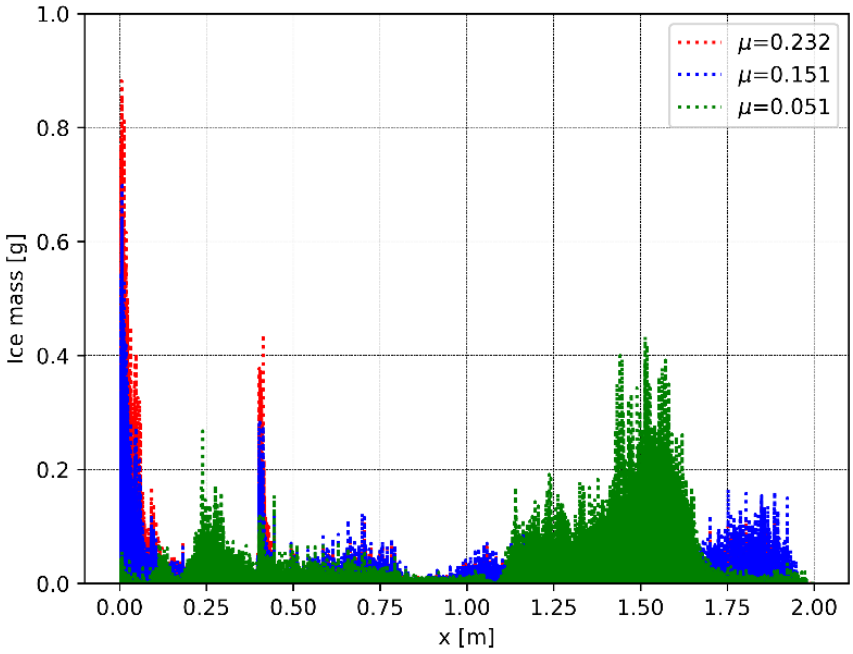

(a)

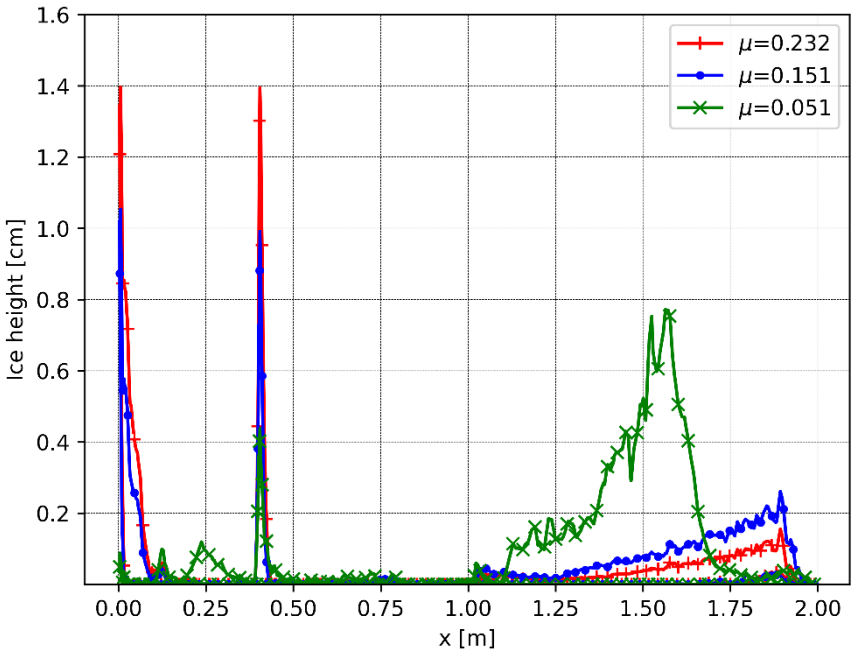

(b)

Fig. 17 Ice accretion mass (top) and ice height at fuselage mid-plane (bottom) for different advance ratios with constant target thrust coefficient (C_T = 0.008).

At the mid-advance ratio, the influence of free stream and wake fuselage interaction effects are both crucial for the ice accretion on the fuselage. The ice accretion on the frontal region and engine intake is influenced by the free stream velocity, as illustrated in Fig. 16 (b) and Fig. 17. In contrast, the ice accretion on the tail boom was due to the wake fuselage interaction.

Another interesting observation was the shift in ice accretion on the tail boom region in the

longitudinal direction with the increase in the advance ratio, as shown in Fig. 17 (red and blue). Further, ice accretion on the side of the fuselage increased with the increase in advance ratio. This is because the velocity of the wake hitting the side of the fuselage at a high advance ratio increases, causing more droplets to deposit, and hence more ice to accrete. As shown in Fig. 18, a non-intuitive pattern of total ice mass for the advance ratio was observed. It shows the highest mass at the lowest advance ratio, then decreases and increases again with the increase in advance ratio.

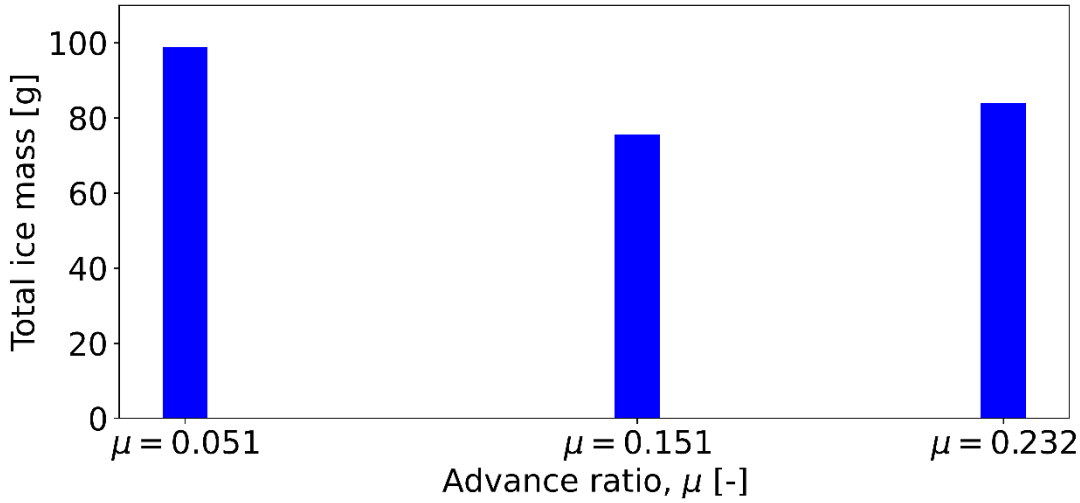

Fig. 18 Total mass of ice accretion for different advance ratios with constant target thrust coefficient (C_T = 0.008).

4.2. Effect of rotor thrust coefficient

(a) Aerodynamic results

The effect of various target rotor thrust coefficients (C_T = 0.004, 0.006, and 0.008 as shown in Table 8) with constant advance ratio (μ = 0.151) was investigated. The target rotor thrust coefficient is the function of collective pitch, lateral cyclic pitch, and longitudinal pitch angles, respectively. Due to the change in blade pitch and rotor plane angles, a different flow field is experienced by the rotorcraft, even though the advance ratio remains identical. The droplet trajectory is dependent on the motion of the carrier phase, that is, air. Fig. 19 shows the wake interaction at various C_T values and when compared with Fig. 12, it is observed that the change in advance ratio has a greater effect on changing the flow field, as compared to the change in the target thrust coefficient. With the increase in C_T, the interaction between rotor wakes and the

fuselage was observed to increase, which is evident from the increase in wake skew angle.

Table 8 Conditions for icing with a fixed advance ratio

Parameter	Value
Advance ratio, μ [-]	0.151
Thrust coefficient, C_T [-]	0.004, 0.006, 0.008
Free stream temperature, T_∞ [K]	258.15
Liquid water content, LWC [g/m^3]	0.6
Median volumetric diameter, MVD [μm]	20.0
Icing time, T_{ice} [minutes]	30.0

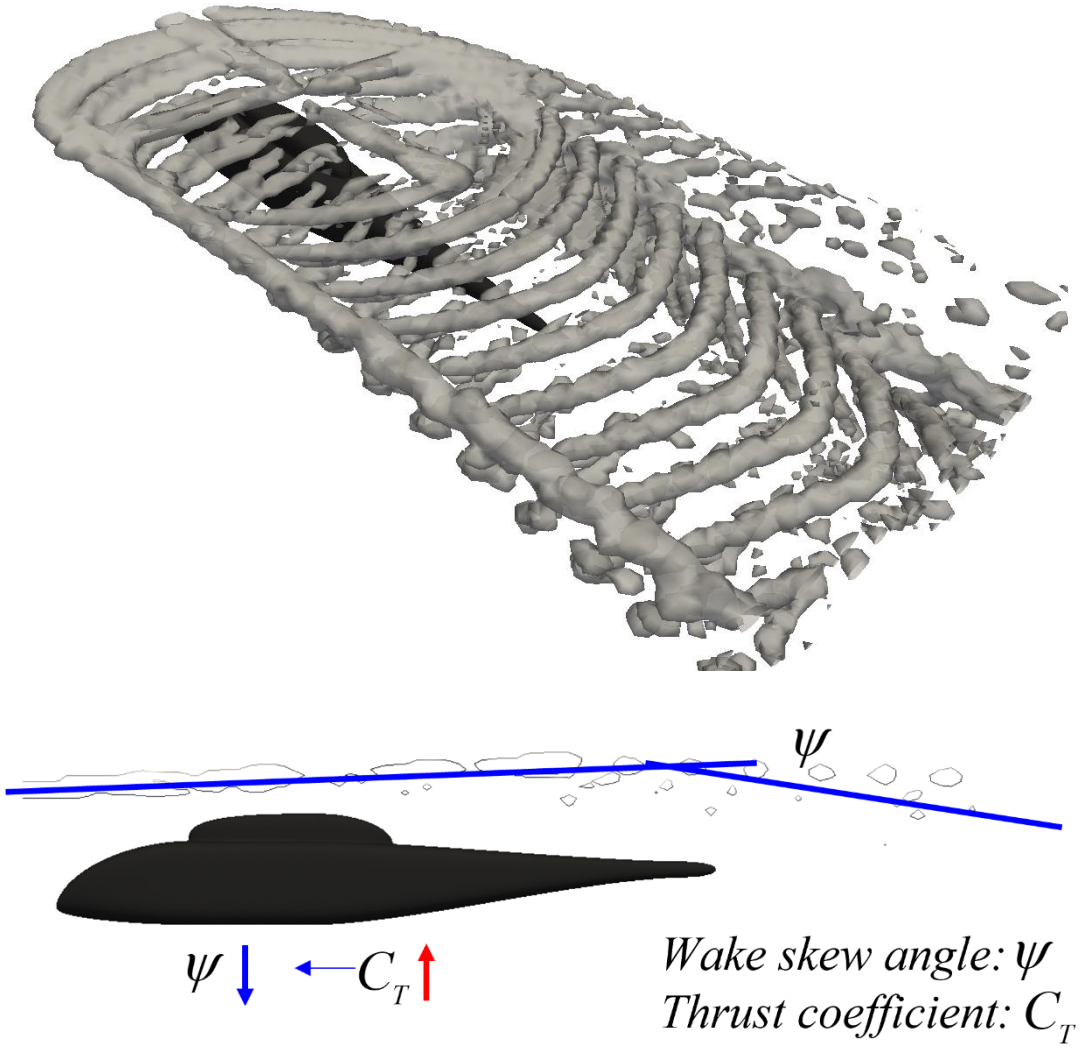

(a) C_T = 0.004.

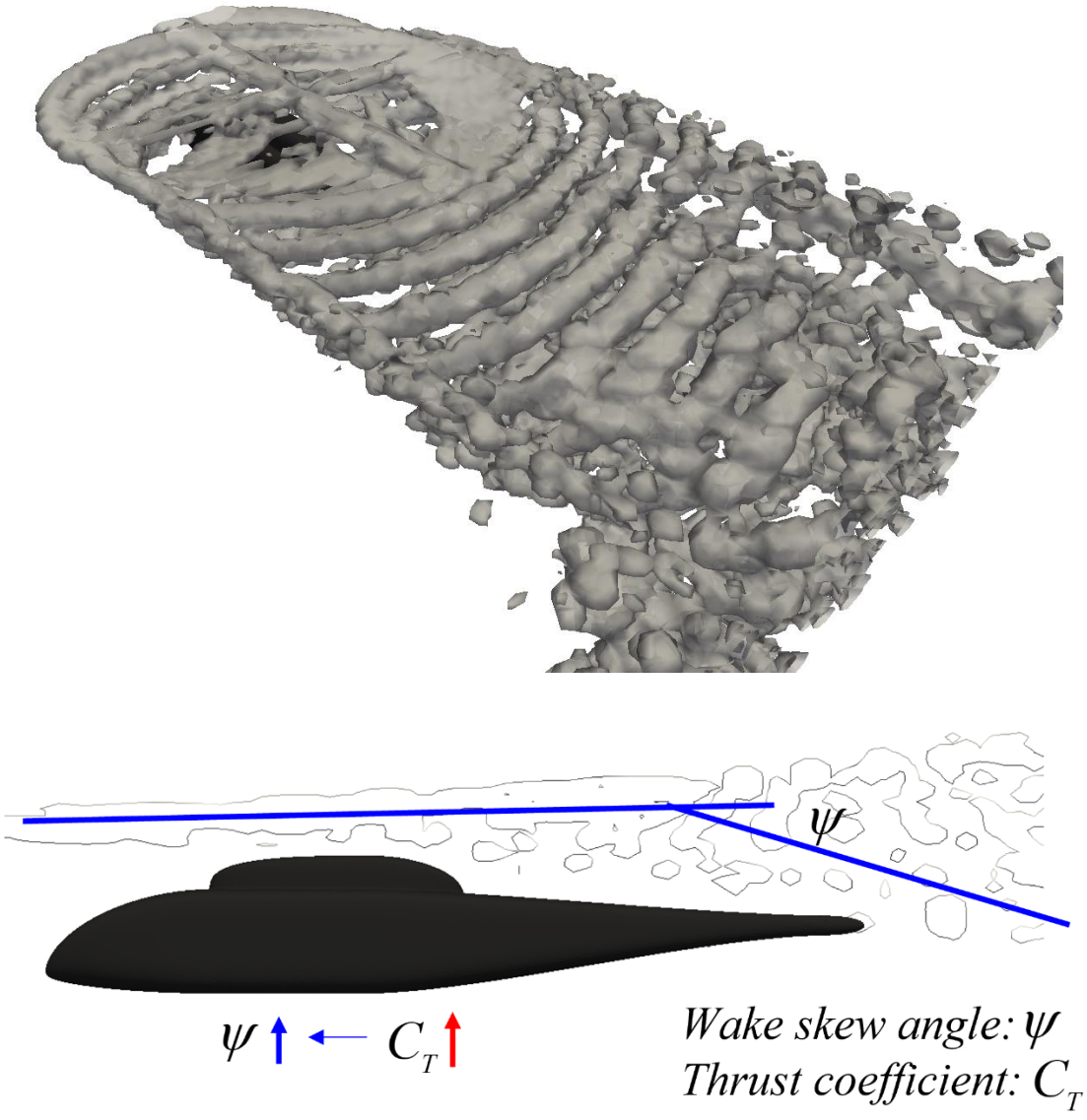

(b) $C_T = 0.006$.

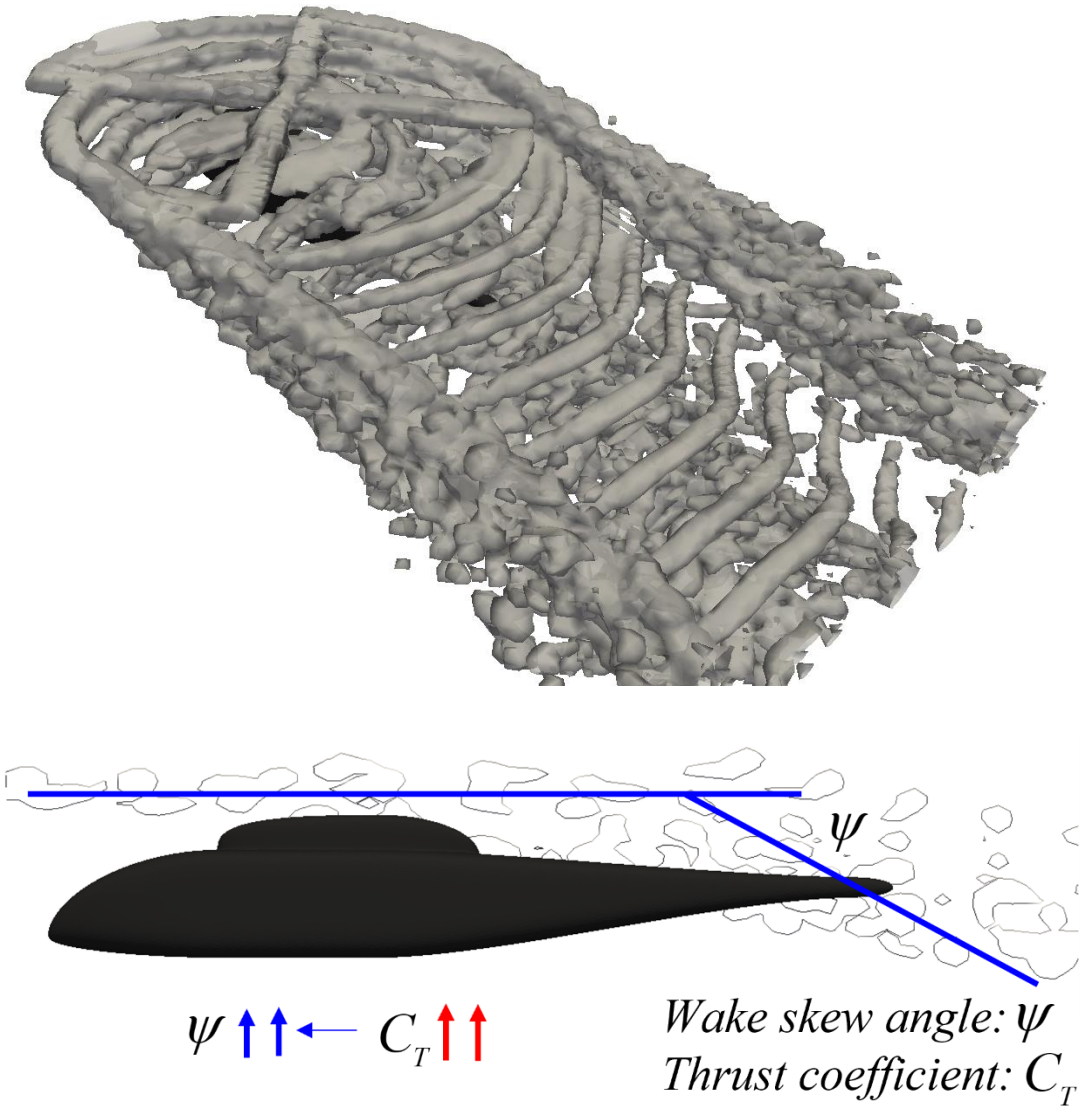

(c) C_T = 0.008.

Fig. 19 The iso-surface at Q=1000 for different target thrust coefficients ((a) C_T = 0.004, (b) C_T = 0.006, and (c) C_T = 0.008) with constant advance ratios (μ = 0.151).

(b) Droplet results

The distribution of collection efficiency with the variation in target thrust coefficient is shown in Fig. 20. As seen from the wake interaction in Fig. 19, the wake near the fairing and tail boom portion had a different interference pattern at different thrust coefficients. The collection efficiency distribution near the nose and engine intake were similar due to the dominant effect of free stream velocity, rather than a wake for different thrust coefficients. The effect of various thrust coefficients was prominent near the fairing and tail boom region, as observed in Fig. 20 (a) and 20 (c). As the thrust coefficient increases, the collective pitch angle has to be increased to maintain

thrust; therefore, more air is pushed through the rotor plane. The resultant free stream air and air pushed through the rotor plane cause greater interaction between the wake with the tail boom at a higher thrust coefficient, than at a lower thrust coefficient. Therefore, more droplets were deposited at the tail boom with a higher rotor thrust coefficient, and lower deposition was found for the low thrust coefficient.

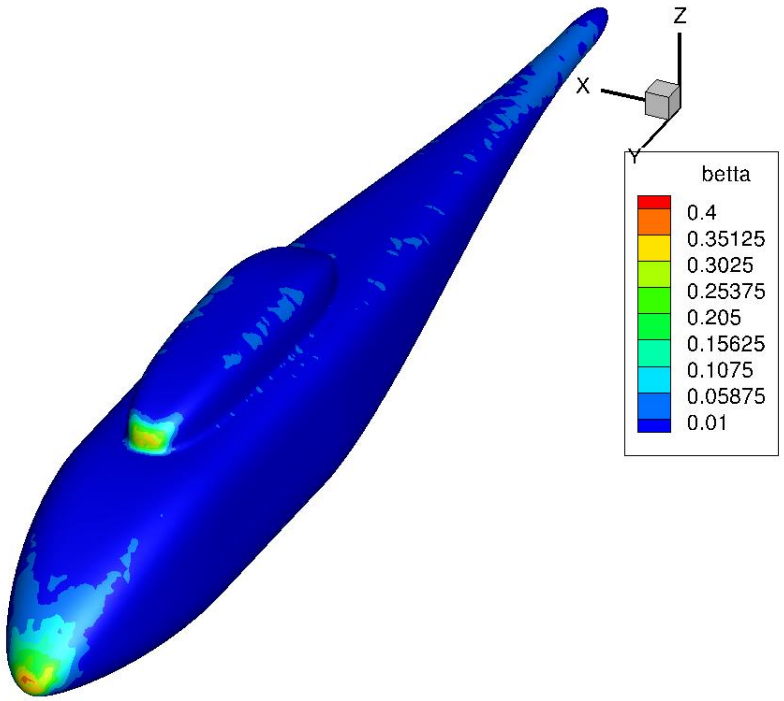

(a) $C_T = 0.004$.

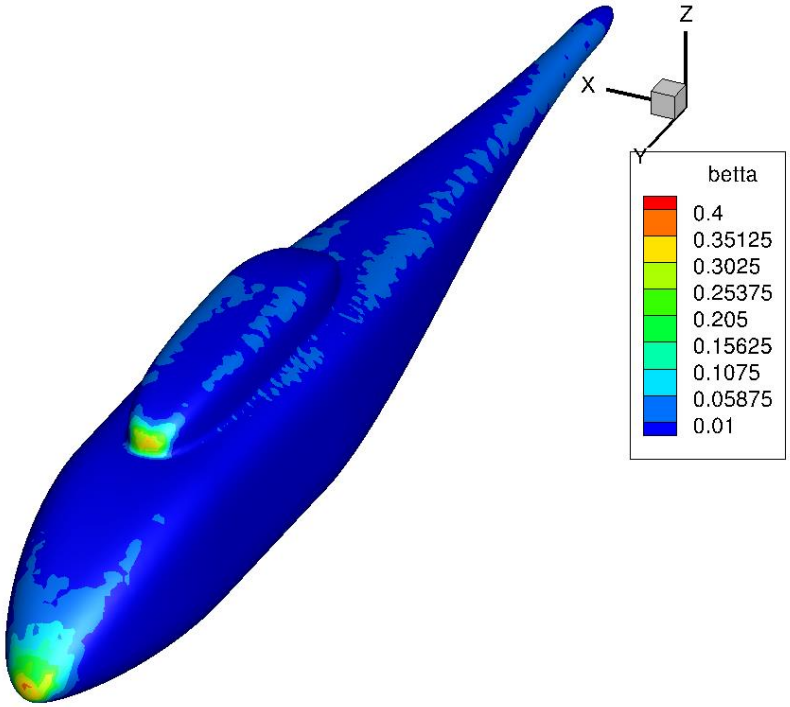

(b) $C_T = 0.006$.

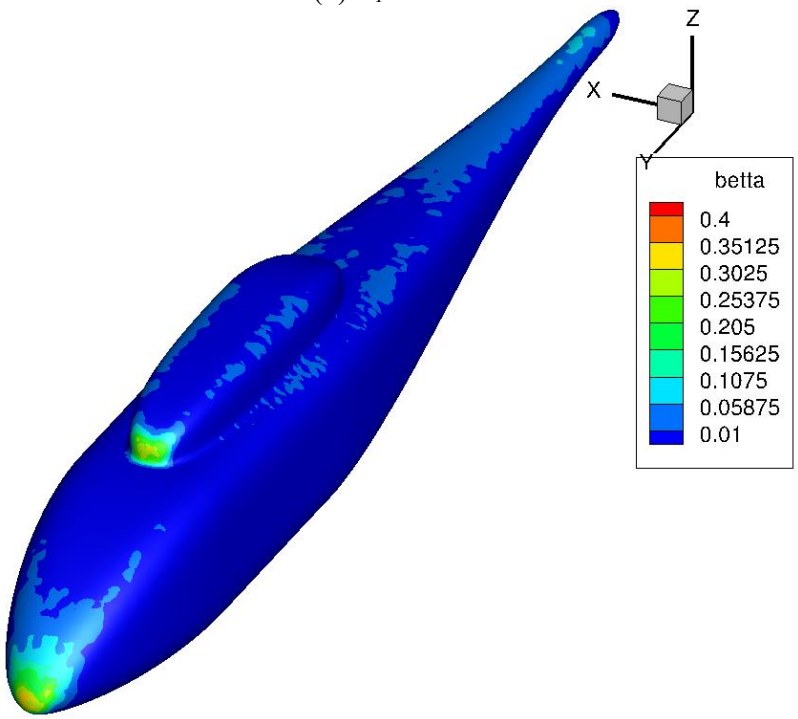

(c) $C_T = 0.008$.

Fig. 20 Collection efficiency for different target thrust coefficients ((a) $C_T = 0.004$, (b) $C_T = 0.006$, and (c) $C_T = 0.008$) with constant advance ratios ($\mu = 0.151$).

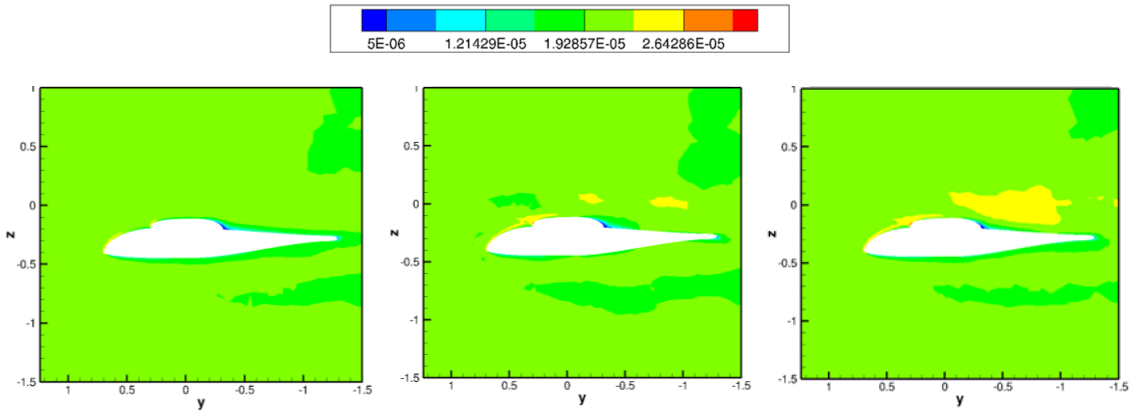

(a) $C_T = 0.004$. (b) $C_T = 0.006$. (c) $C_T = 0.008$.

Fig. 21 The droplet LWC field at different thrust coefficients ($C_T = 0.004$, 0.006, and 0.006, respectively).

Although the streamwise and downwash velocity distribution around the fuselage was similar with various thrust coefficients, the distributions of liquid water content (LWC) were distinctly different for various thrust coefficients. The LWC in the shallow water droplet equation is a sensitive quantity, compared to velocity, which suggests that a small change in the velocity field will result

in an appreciable change in LWC. The LWC distribution near the hub and tail boom wall, shown in Fig. 21, is responsible for the different collection efficiency distributions.

(c) Ice accretion results

As the rotor thrust coefficient increased, the rotor wakes traveled downward due to an increase in blade pitch angle, as can be seen in Fig. 19 for a given advance ratio. Accordingly, the exposure of the tail boom to the wake effect increases, although the frontal region remains the same. Hence, the thrust coefficient is another parameter that determines the rotor wake and fuselage interaction. The effect of the thrust coefficient on the amount and location of ice accretion on the fuselage, for three thrust coefficients (0.004, 0.006, and 0.008), were considered for identical advance ratio and meteorological conditions, as shown in Table 7.

In a high thrust coefficient, the tip vortex collides with the tail boom of the fuselage due to the high blade collective pitch angle. The droplets carried by air through the rotor plane accelerate and impinge on the tail boom and cause icing near the nose, engine intake, and tail boom, as illustrated in Fig. 21. The ice accretion near the nose and engine intake were similar, but the amount and location of ice accretion at the tail boom were significantly different for all the cases, as shown in Fig. 22. Figure 23 (a) and 23 (b) show the total ice mass accretion and ice height at the fuselage center line for the longitudinal direction. Ice height at the tail boom region was observed to be different for all cases, especially for the higher values of thrust coefficient, although the ice mass distribution was nearly identical in all cases.

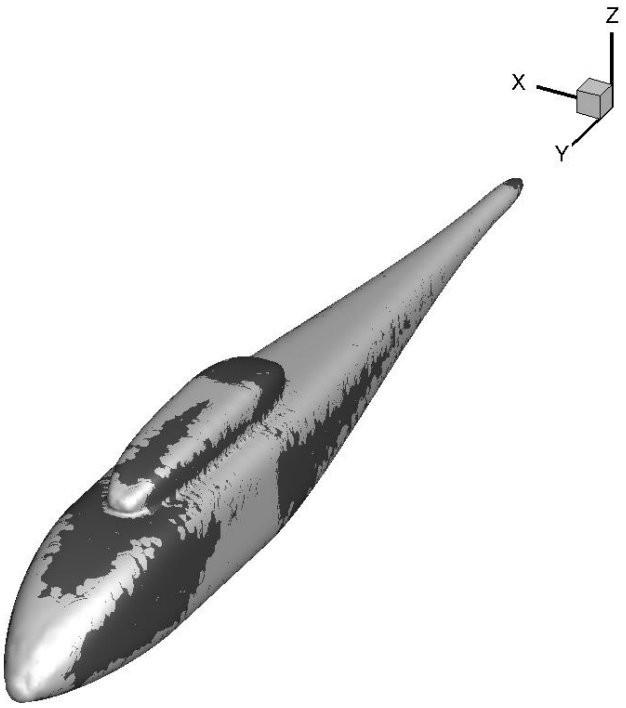

(a) $C_T = 0.004$.

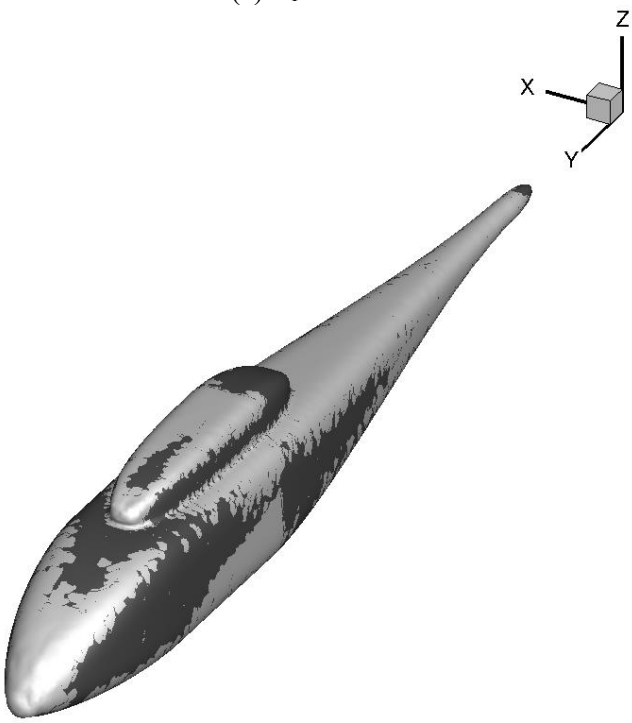

(b) $C_T = 0.006$.

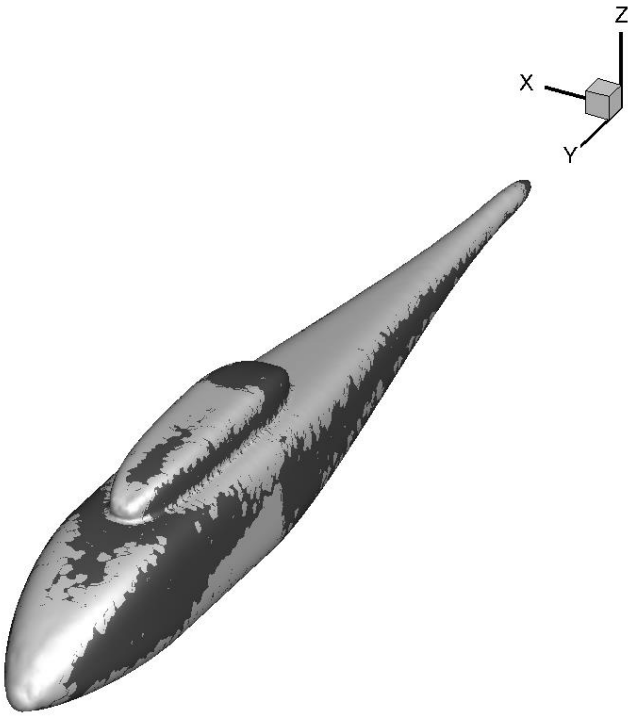

(c) $C_T = 0.008$.

Fig. 22 Ice accretion location for different target thrust coefficients ((a) $C_T = 0.004$, (b) $C_T = 0.006$, and (c) $C_T = 0.008$) with constant advance ratios ($\mu = 0.151$).

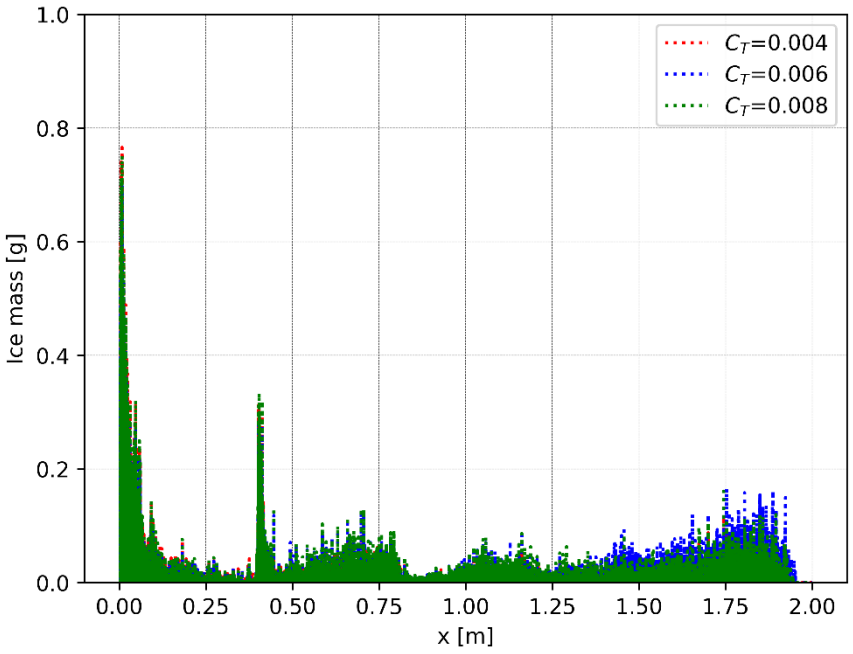

(a)

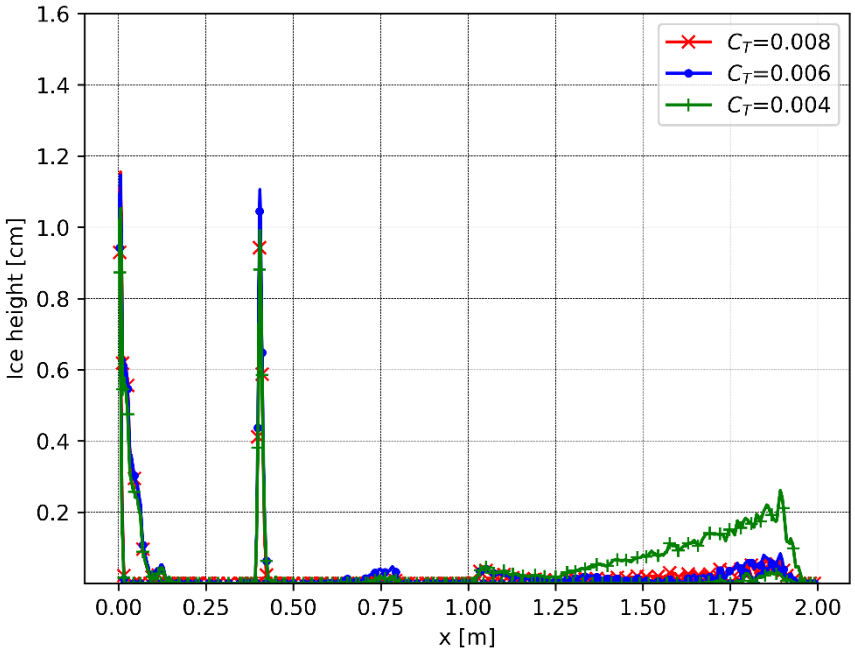

(b)

Fig. 23 Ice accretion mass (top) and ice height at fuselage mid-plane (bottom) for different target thrust coefficients with constant advance ratios (μ = 0.151).

Finally, a comparison was conducted between the methodology utilized by Son *et al*. [19] (left) and the present methodology (right) on ice accretion on the fuselage, for the advance ratio of 0.15 along with the other metrological conditions [19]. The results of the location and ice thickness are compared in Fig. 24. The methodology utilized by Son *et al*. [19] for the aerodynamic prediction was the actuator surface method (ASM). The ASM incorporates the effect of an individual rotor blade as the source term in the momentum equation. The added source term is determined from the calculated thrust for the computed volume of the rotor blade, and it becomes zero for other computed cell volumes. In this way, the source term imposes a pressure jump in the computation cells representing the exact location of the rotor blades.

The present method models wake in the Lagrangian framework and flow around the fuselage in the Eulerian framework with the necessary information exchange between the two. The present solver assumes the convection of wake particles without diffusion. According to Helmholtz's theorem, the strength of the particles emanating from the Kutta wake panel remains constant. The particles have more effect near the engine intake due to their proximity and induce greater velocity due to the rotor blocking the freestream flow field.

Therefore, the velocity in the direction normal to the surface of the engine intake was observed to be less, causing low droplet deposition in the present solver compared to Son *et al*. [19]. Alternately, the particles had less effect on the nose, which enabled the freestream to interact significantly with the fuselage and was observed to have acceleration, due to its shape near the nose. The velocity normal to the surface was more than the former, causing more droplet deposition at the nose. Although some differences were observed between the predictions of ice accretion on the fuselage with the rotor wake effect, the overall trends were similar in both cases.

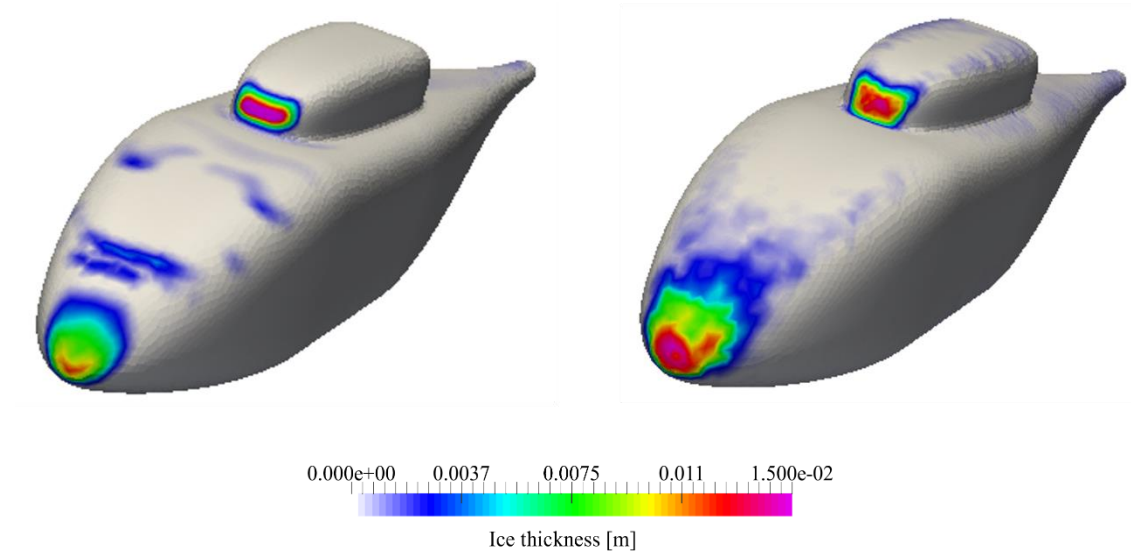

Fig. 24 Comparison of the location and ice thickness between the actuator surface method (left) and the present hybrid method (right).

In this case, with an advance ratio of 0.151 and a thrust coefficient of 0.0065, the ice accretion on a rotorcraft is expected to exhibit specific patterns. Primarily, the thickest ice is expected to form at the stagnation regions of the rotorcraft. For this particular case, the stagnation regions are identified at the nose and engine intake of the rotorcraft. The nose will experience greater ice accretion compared with the engine intake, due to the blocking effect at the engine intake. Moreover, the advance ratio will induce an asymmetrical flow field around the rotorcraft, leading to asymmetric ice accretion. These patterns have been distinctly observed through the application of a hybrid aerodynamic solver, which offers a more nuanced representation of the complex aerodynamics involved and hence predicts more accurate ice accretion.

4.3. Effect of the suction of airflow in the engine intake

Until now, we ignored the effects of the suction of airflow through air intake in the engine intake. To replicate the suction of airflow at the entry of a rotorcraft engine, a special boundary condition involving the target mass flow rate was enforced at the end of the computational domain of the engine intake. The numerical engine intake boundary condition modifies the pressure at a pressure-outlet zone of the engine air intake to achieve the desired mass flow rate. This was accomplished by altering the pressure value at the pressure-outlet zone up and down during each iteration, utilizing Bernoulli's equation of the change in pressure, *dp*, the current and required computed mass flow rates, $\dot{m}$, $\dot{m}_{req}$, the computed average density at the pressure-outlet boundary, ρ_{ave} and the area, A , of the pressure-outlet boundary [16],

$$dp = \frac{\rho_{ave}\left(\dot{m}^2 - \dot{m}_{req}^2\right)}{2\left(\rho_{ave}A\right)^2}. \tag{22}$$

The rotorcraft model considered in this study is taken from the twin-engine Korean Utility Helicopter Surion with Pitot dynamic-type air intakes, primarily developed by Korea Aerospace Industries, LTD. from 2011 to 2024. The target mass flow rate, which generally varies depending on engine operation modes, was set at the end of engine intake in the present study. The interaction between the rotor wake and the engine intake results in a significant degree of asymmetry at the engine intake region.

At a low advance ratio, the influence of the rotor wake on the aerodynamic flow is more significant and the rotor wake encloses the entire fuselage from the nose to the tail. The suction of air inside the engine is very high, and the rotor wake passes through the engine intake and is sucked by the engine, resulting in a high velocity at the passage. The convection of the wake particles predominantly occurs in a downward direction with a high wake-skew angle. It exhibits strong interaction between the rotor wake and fuselage throughout the rotor diameter.

Figure 25 depicts the thickness of ice accretion at low and high advance ratios for the icing condition of LWC of 0.41 g/m^3, MVD of 20 μm, and temperature of 263 K. At low advance ratio, the maximum ice accretion is noted at the fairing region, along with sporadic ice accretion at the tail boom and engine intake, as illustrated in Fig. 25 (a).

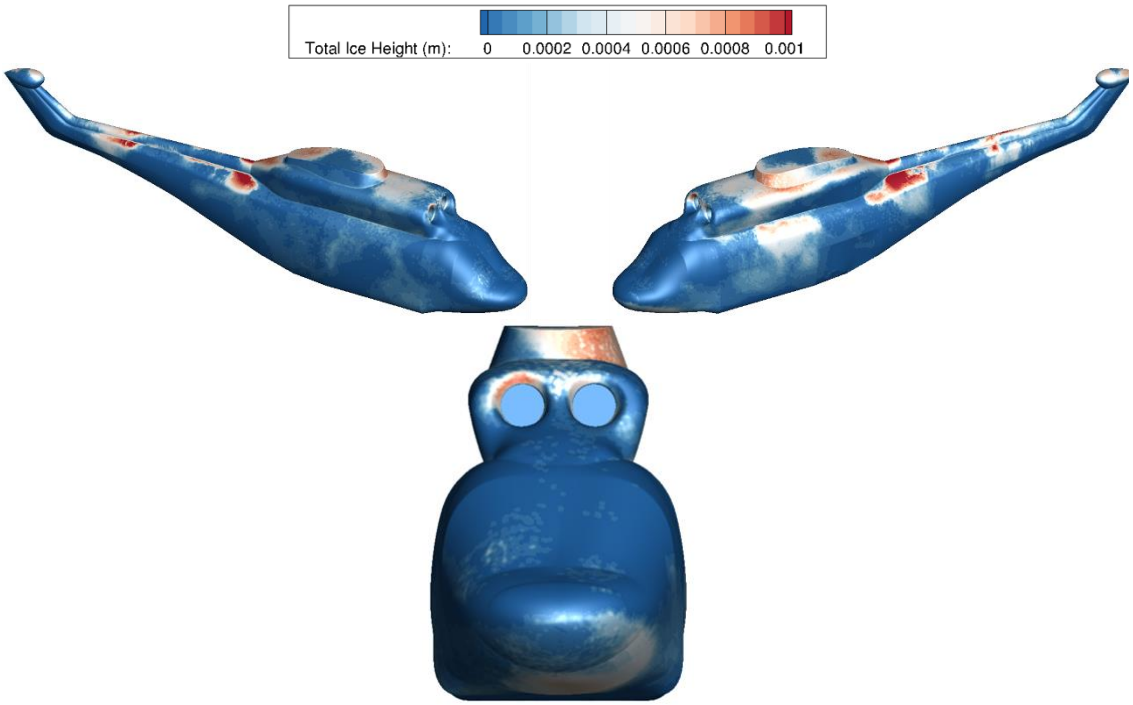

(a)

(b)

Fig. 25. Ice accretion at ‘low’ (a) and ‘high’ (b) advance ratios.

At a high advance ratio, the downstream convection of wake particles occurs due to the high velocity of the free stream. In addition, as the helicopter moves forward at high speeds, the airflow entering the rotor disk is affected by the advancing blade's rotational speed, resulting in higher inflow velocities in the rotor plane's advancing side than the retreating side. This uneven inflow

can cause a swirl or vortex to form at the inlet of the engine intake, creating a blockage effect that reduces the amount of air entering the engine. The velocity field is comparatively more symmetric as compared to the low advance ratio case. Significant ice accretion is observed at the engine intake, windshield, and nose region, while minimal ice accretion is observed at the tail boom and fin region. This phenomenon can be attributed to the counteractive influence of the freestream and rotor wake.

As shown in Fig. 25 (b), at the high advance ratio, a considerable amount of ice accretion is observed at the front of the fuselage and the end region of the tail boom and fin. The ice accretion at the front region of the fuselage is due to the interaction of freestream flow with the fuselage, which deposits a large amount of the droplets on this region of the fuselage. At the same time, due to high freestream velocity, the rotor wake is convected downstream, causing an interaction and a large ice accretion at the end portion of the tail boom and fin region.

4.4. Comparison between without rotor and with rotor

Since the full-body analysis or the experimental test using an icing wind tunnel of a rotorcraft considering the rotor blade and its shape effects in detail is very complicated, for convenience, the downwash effect of the rotor is often imitated by applying an angle of side slip. To correctly use the results based on the side slip approach, it is necessary to investigate the differences between ice accretion with the rotor and without the rotor.

The ice shapes are compared in Fig. 26 (a) and 27 (a) for the case without a rotor and in Fig. 26 (b) and 27 (b) for the case with a rotor for low and high advance ratios, respectively. At a low advance ratio, it is evident from Fig. 26 (b) that the fairing region of the fuselage and engine inlet experienced significant asymmetric ice accretion, whereas there was practically no ice accretion at the fairing region and little ice accretion at the engine inlet in the case without rotor system as shown in Fig. 26 (a). Ice accretion on the engine inlet and the downside of the fuselage's nose is evident in Fig. 26 (b). However, due to the rotor wake effects at high advance ratio, the windshield region was completely covered with ice because of the interaction between freestream and rotor downwash, as shown in Fig. 27 (b), in contrast to ice accretion without rotor where the accretion is observed at the sides of the windshield and the nose as shown in Fig. 27 (a).

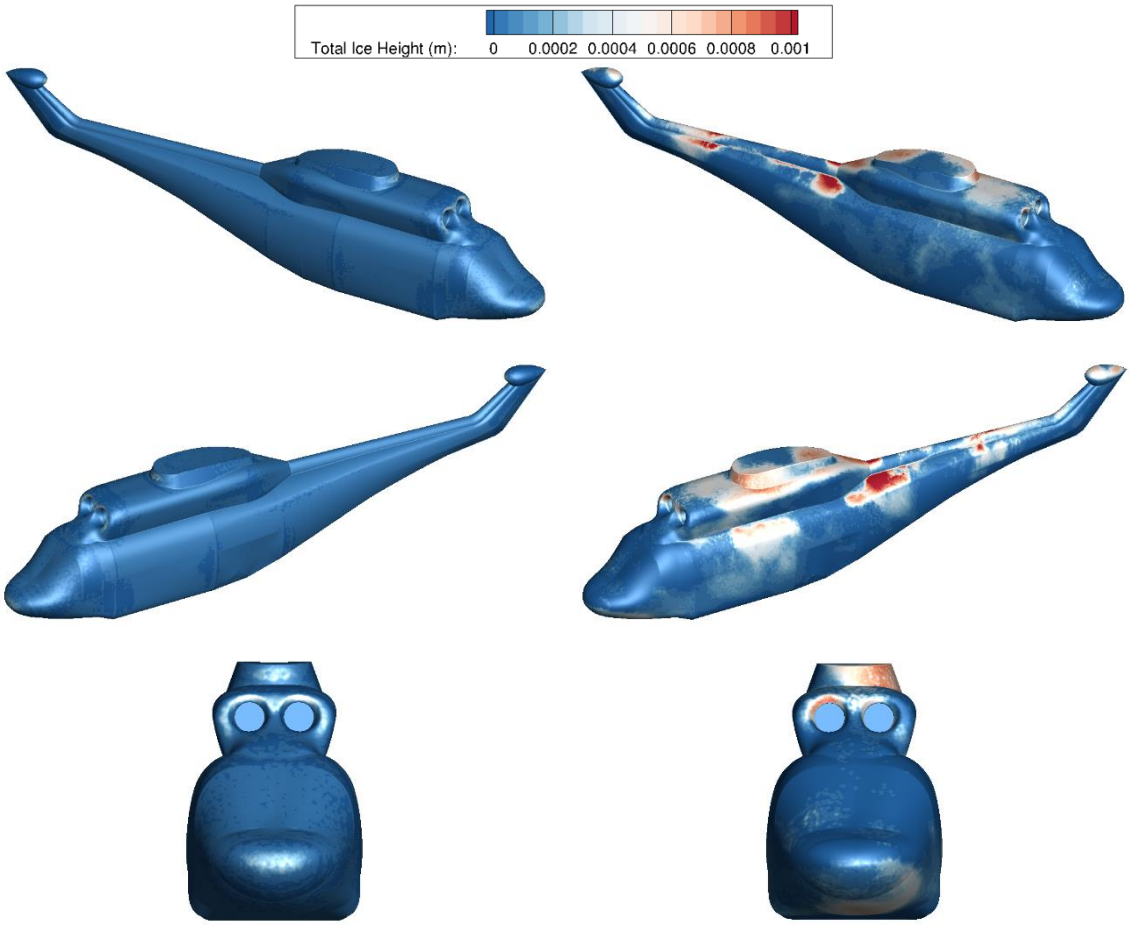

(a) (b)

Fig. 26. Comparison of ice accretion between without rotor (a) and with rotor (b) at a low advance ratio.

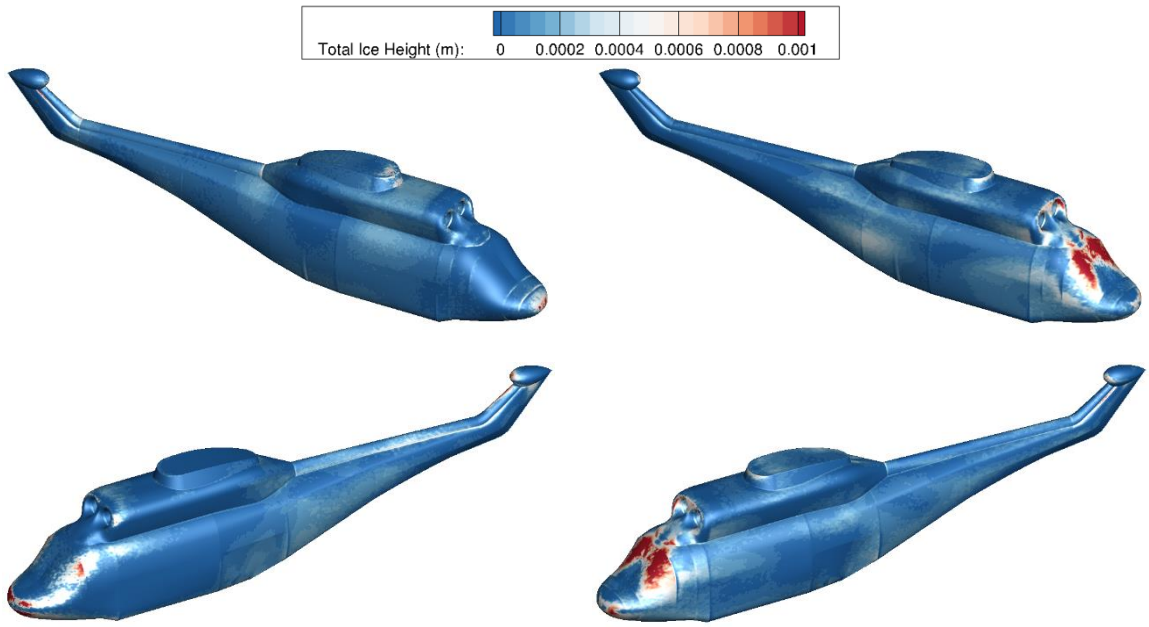

(a) (b)

Fig. 27. Comparison of ice accretion between without rotor (a) and with rotor (b) at a high advance ratio.

5. Conclusions

Simulating ice accretion on a rotorcraft fuselage is computationally expensive in terms of time and resources. Among all available solvers, the aerodynamic solver is the most expensive module. Several methodologies can be used to compute flow fields around rotorcraft, such as high-fidelity CFD methods, combinations with actuator disk models, actuator surface methods, or vortex methods. High-fidelity CFD methods using overset or dynamic grids to solve the flow field around the rotor are computationally very expensive and still suffer from the numerical diffusion of wakes away from rotors. Actuator disk models and actuator surface methods are efficient methods compared to the former but have a fine grid requirement away from the fuselage to preserve wake structure and minimize numerical wake diffusion. Vortex methods are very efficient methods, well suited for predicting the rotorcraft flow field, but not ideal for ice accretion simulations. As all the vortex methods are based on potential flow theory, they have serious limitations when computing wall shear stress and heat flux, which are required in icing calculations. Although there are a few approaches to calculating wall properties, they are empirical and case-dependent.

The present hybrid method has the advantages of both the Lagrangian and Eulerian frameworks. Lagrangian and Eulerian frameworks were adopted to describe the rotor wakes and flow fields around the fuselage, respectively. Using the Lagrangian description of wake, no artificial or numerical diffusion of wakes is encountered, which preserves the wake structure independently of the Eulerian grid. At the same time, as the flow field is described in the Eulerian framework, nonlinear flow phenomenon can be captured, and wall properties can be naturally computed, unlike vortex methods.

The present method also has the advantage of needing less computational resources and time while providing adequate accuracy. The hybrid method showed a significant improvement in computing speed by more than 8 times compared to the existing method based on an overset mesh. The hybrid method was validated using a ROBIN rotorcraft system, and predicted pressure coefficients on the fuselage with reasonable accuracy, providing better agreement with experiments than other numerical methods. A finite volume method was used to solve the shallow water-based droplet equations. Further, a PDE-based ice accretion solver was developed to predict the ice shapes on the clean geometry under ambient icing conditions.

The solvers were utilized with the ROBIN rotorcraft to compute the flow fields for different flow conditions, with varying advance ratios and rotor target thrust coefficients, to study their effect on ice accretion. After the convergence of the rotor target thrust coefficient by trimming, the aerodynamic flow field was averaged over an entire revolution. The averaged flow field from the aerodynamic solver was used to initialize the droplet solver to calculate the impingement limit by collection efficiency. The ice accretion locations and amounts were predicted by the ice accretion solver.

In this study, it was observed that the advance ratio had a significant effect on the ice accretion location and accreted mass. At a lower advance ratio, the frontal region of the fuselage and tail boom region had significant icing, while at a high advance ratio, the stagnation regions, such as the nose and engine intake, were exposed to high ice accretion. Ice accretion in the tail boom region was greater for high rotor thrust coefficients because there was more interaction between the wake and tail boom.

Effect of the suction of airflow in the engine intake on ice accretion was found significant. At a low advance ratio, the maximum ice accretion is noted at the fairing region, along with sporadic ice accretion at the tail boom and engine intake. On the other hand, at the high advance ratio, a considerable amount of ice accretion is observed at the front of the fuselage (due to the strong interaction of freestream flow with the fuselage) and the end region of the tail boom and fin (due to strong downstream convection of the rotor wake).

Since the current method is a general methodology that can be applied to a configuration

significantly different from that of conventional rotorcraft, it can be applied to the study of wake dynamics and ice accretion around compound rotorcraft or multirotor aircraft. It will be interesting to investigate rotor-wake, wake-wake, and wake-fuselage interactions, and their effects on aerodynamics and icing.

Acknowledgments

This work was supported by the National Research Foundation of Korea (NRF) Grant (RS-2024-00397400) and Regional Innovation Mega Project Program (2023-DD-UP-0026) through the Korea Innovation Foundation funded by the Ministry of Science and ICT, South Korea.

References

[1] Raj, L. P., Lee, J., and Myong, R. S., "Ice Accretion and Aerodynamic Effects on a Multi-Element Airfoil Under SLD Icing Conditions," *Aerospace Science and Technology*, Vol. 85, Feb. 2019, pp. 320–333. doi: https://doi.org/10.1016/j.ast.2018.12.017

[2] Raj, L. P., Yee, K., and Myong, R. S., "Sensitivity of Ice Accretion and Aerodynamic Performance Degradation to Critical Physical and Modeling Parameters Affecting Airfoil Icing," *Aerospace Science and Technology*, Vol. 98, Mar. 2020, Paper No. 105659. doi: https://doi.org/10.1016/j.ast.2019.105659

[3] Sengupta, B., Raj, L. P., Cho, M., Son, C., Yoon, T., Yee, K., and Myong, R. S., "Computational Simulation of Ice Accretion and Shedding Trajectory of a Rotorcraft in Forward Flight with Strong Rotor Wakes," *Aerospace Science and Technology*, Vol. 119, Dec. 2021, Paper No. 107140. doi: https://doi.org/10.1016/j.ast.2021.107140

[4] Cao, Y., and Chen, K., "Helicopter Icing," *Aeronautical Journal*, Vol. 114, No. 1152, 2010, pp. 83–90. doi: https://doi.org/10.1017/S0001924000003559

[5] Raj, L. P., Esmaeilifar, E., Jeong, H., and Myong, R. S., "Computational Simulation of Glaze Ice Accretion on a Rotorcraft Engine Intake in Large Supercooled Droplet Icing Conditions," *AIAA 2022-0447*, AIAA SciTech 2022 Forum, 2022. doi: https://doi.org/10.2514/6.2022-0447

[6] Perry, D., "AW609 Certification Slips Again to End-2019," *FlightGlobal*, 2018.

[7] Min, S., and Yee, K., "New Roughness-Induced Transition Model for Simulating Ice Accretion on Airfoils," *AIAA Journal*, Vol. 59, Dec. 2021, pp. 250–262. doi: https://doi.org/10.2514/1.J059222

[8] Xiao, M., Zhang, Y., and Zhou, F., "Numerical Investigation of the Unsteady Flow Past an Iced Multi-Element Airfoil," *AIAA Journal*, Vol. 58, May 2020, pp. 3848–3862. doi: https://doi.org/10.2514/1.J059114

[9] Han, Y., and Palacios, J., "Airfoil-Performance-Degradation Prediction Based on Nondimensional Icing Parameters," *AIAA Journal*, Vol. 51, Nov. 2013, pp. 2570–2581. doi: https://doi.org/10.2514/1.J052207

[10] Coffman, H., "Helicopter Rotor Icing Protection Methods," *Journal of the American Helicopter Society*, Vol. 32, Apr. 1987, pp. 34–39. doi: https://doi.org/10.4050/JAHS.32.34

[11] Rosen, K., and Potash, M., "Forty Years of Helicopter Ice Protection Experience at Sikorsky

Aircraft," *Journal of the American Helicopter Society*, Vol. 26, July 1981, pp. 5–19. doi: https://doi.org/10.2514/6.1981-407

[12] Esmaeilifar, E., Raj, L. P., and Myong, R. S., "Computational Simulation of Aircraft Electrothermal De-Icing Using an Unsteady Formulation of Phase Change and Runback Water in a Unified Framework," *Aerospace Science and Technology*, Vol. 130, Nov. 2022, Paper No. 107936. doi: https://doi.org/10.1016/j.ast.2022.107936

[13] Szilder, K., "Numerical Simulation of Ice Formation on a Helicopter Fuselage," *SAE TP 2007-01-3308*, 2007. doi: https://doi.org/10.4271/2007-01-3308

[14] Szilder, K., and Lozowski, E., "Numerical Simulation of Cloud Drop Impingement on a Helicopter," *27th Congress of the Aeronautical Sciences*, ICAS, Nice, France, 2010.

[15] Aliaga, C. N., Aubé, M. S., Baruzzi, G. S., and Habashi, W. G., "FENSAP-ICE-Unsteady: Unified In-Flight Icing Simulation Methodology for Aircraft, Rotorcraft, and Jet Engines," *Journal of Aircraft*, Vol. 48, Jan. 2011, pp. 119–126. doi: https://doi.org/10.2514/1.C000327

[16] Ahn, G. B., Jung, K. Y., Myong, R. S., Shin, H. B., and Habashi, W. G., "Numerical and Experimental Investigation of Ice Accretion on Rotorcraft Engine Air Intake," *Journal of Aircraft*, Vol. 52, Feb. 2015, pp. 903–909. doi: https://doi.org/10.2514/1.C032839

[17] Fouladi, H., Habashi, W. G., and Ozcer, I. A., "Quasi-Steady Modeling of Ice Accretion on a Helicopter Fuselage in Forward Flight," *Journal of Aircraft*, Vol. 50, July 2013, pp. 1169–1178. doi: https://doi.org/10.2514/1.C032096

[18] Leishman, G. J., *Principles of Helicopter Aerodynamics with CD Extra*, Cambridge University Press, Cambridge, England, 2006.

[19] Son, C., Oh, S., and Yee, K., "Ice Accretion on Helicopter Fuselage Considering Rotor-Wake Effects," *Journal of Aircraft*, Vol. 54, Aug. 2017, pp. 500–518. doi: https://doi.org/10.2514/1.C033830

[20] Kim, T., Oh, S., and Yee, K., "Improved Actuator Surface Method for Wind Turbine Application," *Renewable Energy*, Vol. 76, Apr. 2015, pp. 16–26. doi: https://doi.org/10.1016/j.renene.2014.11.002

[21] O'Brien, D. M. Jr., "Analysis of Computational Modeling Techniques for Complete Rotorcraft Configurations," Ph.D. Dissertation, Georgia Institute of Technology, Atlanta, GA, 2006.

[22] Bae, E. S., Rand, P., and He, C., "Hybrid Lagrangian-Eulerian Approach for Modeling Aerodynamic Interactions," *AIAA 2019-3474*, AIAA Aviation 2019 Forum, 2019. doi: https://doi.org/10.2514/6.2019-3474

[23] He, C., and Rajmohan, N., "Modeling the Aerodynamic Interaction of Multiple Rotor Vehicles and Compound Rotorcraft with Viscous Vortex Particle Method," *Proceedings of AHS 72nd Annual Forum*, American Helicopter Society International, West Palm Beach, FL, 2016.

[24] Rajmohan, N., and He, C., "A VPM/CFD Coupling Methodology to Study Rotor/Ship Aerodynamic Interaction," *AIAA 2016-1915*, AIAA Modeling and Simulation Technologies Conference, 2016. doi: https://doi.org/10.2514/6.2016-1915

[25] Quon, E. W., Smith, M. J., Whitehouse, G. R., and Wachspress, D., "Unsteady Reynolds-Averaged Navier-Stokes-Based Hybrid Methodologies for Rotor-Fuselage Interaction," *Journal of Aircraft*, Vol. 49, May 2012, pp. 961–965. doi: https://doi.org/10.2514/1.C031578

[26] Sugiura, M., Tanabe, Y., Saito, S., Sugawara, H., Ohshio, K., and Kanazaki, M., "Hybrid Method of CFD and Prescribed Wake Model for Rotorcraft Aeroacoustics and Aerodynamics Prediction," *38th European Rotorcraft Forum*, CEAS, Amsterdam, Netherlands, 2012. doi: https://doi.org/10.2322/tjsass.56.343

[27] Papadakis, M., Yeong, H. W., Wong, S. C., Vargas, M., and Potapczuk, M., "Experimental Investigation of Ice Accretion Effects on a Swept Wing," *DOT/FAA/AR-05/39*, Federal Aviation Administration, 2005.

[28] Raj, L. P., Esmaeilifar, E., Sengupta, B., Jeong, H., and Myong, R., "Coarray Fortran Parallel Implementation of a Finite Volume Method-Based Aircraft Ice Accretion Simulation Code," *International Journal of Aeronautical and Space Sciences*, Vol. 24, No. 4, 2023, pp. 1124–1135. doi: https://doi.org/10.1007/s42405-023-00601-8

[29] Johnson, W., *Rotorcraft Aeromechanics*, Cambridge University Press, 2013. doi: https://doi.org/10.1017/CBO9781139235655

[30] Landgrebe, A. J., Moffitt, R. C., and Clark, D. R., "Aerodynamic Technology for Advanced Rotorcraft—Part I," *Journal of the American Helicopter Society*, Vol. 22, Apr. 1977, pp. 21–27. doi: https://doi.org/10.4050/JAHS.22.21

[31] Landgrebe, A. J., Moffitt, R. C., and Clark, D. R., "Aerodynamic Technology for Advanced Rotorcraft—Part II," *Journal of the American Helicopter Society*, Vol. 22, July 1977, pp. 2–9. doi: https://doi.org/10.4050/JAHS.22.21

[32] DeYoung, J., "Historical Evolution of Vortex-Lattice Methods," *N76-28164*, NASA Langley Research Center, *Vortex-Lattice Utilization*, 1976.

[33] Katz, J., and Maskew, B., "Unsteady Low-Speed Aerodynamic Model for Complete Aircraft Configurations," *Journal of Aircraft*, Vol. 25, May 1988, pp. 302–310. doi: https://doi.org/10.2514/3.45564

[34] Quackenbush, T., Lam, C. M., and Bliss, D., "Vortex Methods for the Computational Analysis of Rotor/Body Interaction," *Journal of the American Helicopter Society*, Vol. 39, Oct. 1994, pp. 14–24. doi: https://doi.org/10.4050/JAHS.39.14

[35] Rubbert, P., and Saaris, G., "A General Three-Dimensional Potential-Flow Method Applied to V/STOL Aerodynamics," *SAE Transactions*, 1968, pp. 945–957. doi: https://doi.org/10.4271/680304

[36] Hess, J. L., "Calculation of Potential Flow About Arbitrary Three-Dimensional Lifting Bodies," *Douglas Aircraft Co.*, Long Beach, CA, 1972.

[37] Crispin, Y., "Unsteady Rotor Aerodynamics Using a Vortex Panel Method," *9th Atmospheric Flight Mechanics Conference*, 1982. doi: https://doi.org/10.2514/6.1982-1348

[38] Zhao, J., He, C., Zhang, L., Zhao, H., and Hu, P., "Coupled Viscous Vortex Particle Method and Unstructured Computational Fluid Dynamics Solver for Rotorcraft Aerodynamic Interaction Analysis," *AIAA 2011-1121*, 49th AIAA Aerospace Sciences Meeting Including the New Horizons Forum and Aerospace Exposition, 2011. doi: https://doi.org/10.2514/6.2011-1121

[39] Lee, H., and Lee, D.-J., "Effects of Platform Motions on Aerodynamic Performance and Unsteady Wake Evolution of a Floating Offshore Wind Turbine," *Renewable Energy*, Vol. 143, Dec 2019, pp. 9–23. doi: https://doi.org/10.1016/j.renene.2019.04.134

[40] Jo, Y., Lee, H., and Lee, D., "Prediction of Rotor Flow for Unmanned Aerial System Using Nonlinear Vortex Lattice Method," *6th Asia/Australian Rotorcraft Forum/Heli Japan*, AA-RF, Kanazawa, Japan, 2017.

[41] Lee, H., and Lee, D.-J., "Numerical Investigation of the Aerodynamics and Wake Structures of Horizontal Axis Wind Turbines by Using Nonlinear Vortex Lattice Method," *Renewable Energy*, Vol. 132, Mar. 2019, pp. 1121–1133. doi: https://doi.org/10.1016/j.renene.2018.08.087

[42] Proulx-Cabana, V., Nguyen, M. T., Prothin, S., Michon, G., and Laurendeau, E., "A Hybrid Non-Linear Unsteady Vortex Lattice-Vortex Particle Method for Rotor Blades Aerodynamic Simulations," *Fluids*, Vol. 7, No. 2, 2022, Paper No. 81. doi:

https://doi.org/10.3390/fluids7020081

[43] Samad, A., Tagawa, G. B., Morency, F., and Volat, C., "Predicting Rotor Heat Transfer Using the Viscous Blade Element Momentum Theory and Unsteady Vortex Lattice Method," *Aerospace*, Vol. 7, No. 7, 2020, Paper No. 90. doi: https://doi.org/10.3390/aerospace7070090

[44] Lee, H., "Development of Nonlinear Vortex Lattice Method for Predicting Wind Turbine Performance and Wake Structures," Ph.D. Thesis, KAIST, 2019.

[45] Lee, H., and Lee, D.-J., "Wake Impact on Aerodynamic Characteristics of Horizontal Axis Wind Turbine Under Yawed Flow Conditions," *Renewable Energy*, Vol. 136, June 2019, pp. 383–392. doi: https://doi.org/10.1016/j.renene.2018.12.126

[46] Lee, H., Sengupta, B., Araghizadeh, M. S., and Myong, R. S., "Review of Vortex Methods for Rotor Aerodynamics and Wake Dynamics," *Advances in Aerodynamics*, Vol. 4, May 2022, pp. 1–36. doi: https://doi.org/10.1186/s42774-022-00111-3

[47] Sengupta, B., Lee, Y., Araghizadeh, M. S., Myong, R. S., and Lee, H., "Comparative Analysis of Direct Method and Fast Multipole Method for Multirotor Wake Dynamics," *International Journal of Aeronautical and Space Sciences*, Jan. 2024. doi: https://doi.org/10.1007/s42405-023-00699-w

[48] Lee, H., and Lee, D.-J., "Rotor Interactional Effects on Aerodynamic and Noise Characteristics of a Small Multirotor Unmanned Aerial Vehicle," *Physics of Fluids*, Vol. 32, Apr. 2020, Paper No. 047107. doi: https://doi.org/10.1063/5.0003992

[49] Lee, H., and Lee, D.-J., "Low Reynolds Number Effects on Aerodynamic Loads of a Small Scale Wind Turbine," *Renewable Energy*, Vol. 154, July 2020, pp. 1283–1293. doi: https://doi.org/10.1016/j.renene.2020.03.097

[50] Winckelmans, G. S., "Topics in Vortex Methods for the Computation of Three-and Two-Dimensional Incompressible Unsteady Flows," *California Institute of Technology*, USA, 1989. doi: https://doi.org/10.7907/19HD-DF80

[51] Cottet, G.-H., and Koumoutsakos, P. D., *Vortex Methods: Theory and Practice*, Cambridge University Press, 2000. doi: https://doi.org/10.1088/0957-0233/12/3/704

[52] Winckelmans, G., and Leonard, A., "Contributions to Vortex Particle Methods for the Computation of Three-Dimensional Incompressible Unsteady Flows," *Journal of Computational Physics*, Vol. 109, Dec. 1993, pp. 247–273. doi: https://doi.org/10.1006/jcph.1993.1216

[53] Wright, W., Al-Khalil, K., and Miller, D., "Validation of NASA Thermal Ice Protection Computer Codes. II-LEWICE/Thermal," *AIAA 97-0050*, 35th Aerospace Sciences Meeting and Exhibit, 1997. doi: https://doi.org/10.2514/6.1997-50

[54] Villedieu, P., Trontin, P., Guffond, D., and Bobo, D., "SLD Lagrangian Modeling and Capability Assessment in the Frame of ONERA 3D Icing Suite," *AIAA 2012-3132*, 4th AIAA Atmospheric and Space Environments Conference, 2012. doi: https://doi.org/10.2514/6.2012-3132

[55] Durst, F., Milosevic, D., and Schönung, B., "Eulerian and Lagrangian Predictions of Particulate Two-Phase Flows: A Numerical Study," *Applied Mathematical Modelling*, Vol. 8, Apr. 1984, pp. 101–115. doi: https://doi.org/10.1016/0307-904X(84)90062-3

[56] Bourgault, Y., Habashi, W. G., Dompierre, J., and Baruzzi, G. S., "A Finite Element Method Study of Eulerian Droplets Impingement Models," *International Journal of Numerical Methods in Fluids*, Vol. 29, Mar. 1999, pp. 429–449. doi: https://doi.org/10.1002/(SICI)1097-0363(19990228)29:4<429::AID-FLD795>3.0.CO;2-F

[57] Jung, S. K., and Myong, R. S., "A Second-Order Positivity-Preserving Finite Volume Upwind Scheme for Air-Mixed Droplet Flow in Atmospheric Icing," *Computers & Fluids*, Vol. 86, Nov.

2013, pp. 459–469. doi: https://doi.org/10.1016/j.compfluid.2013.08.001

[58] Jung, S. K., Myong, R. S., and Cho, T. H., "Development of Eulerian Droplets Impingement Model Using HLLC Riemann Solver and POD-Based Reduced Order Method," *AIAA 2011-3907*, 41st AIAA Fluid Dynamics Conference and Exhibit, 2011. doi: https://doi.org/10.2514/6.2011-3907

[59] Lapple, C., *Fluid and Particle Mechanics*, Vincent Press, USA, 2007.

[60] Cao, Y., Zhang, Q., and Sheridan, J., "Numerical Simulation of Rime Ice Accretions on an Aerofoil Using an Eulerian Method," *Aeronautical Journal*, Vol. 112, Feb. 2008, pp. 243–249. doi: https://doi.org/10.1017/S0001924000002189

[61] Norde, E., Hospers, J. M., Van Der Weide, E., and Hoeijmakers, H. W., "Aircraft Icing in Flight: Effects of Impact of Supercooled Large Droplets," *29th Congress of the International Council of the Aeronautical Sciences*, International Council of the Aeronautical Sciences (ICAS), Russia, 2014.

[62] Messinger, B. L., "Equilibrium Temperature of an Unheated Icing Surface as a Function of Air Speed," *Journal of the Aeronautical Sciences*, Vol. 20, Aug. 1953, pp. 29–42. doi: https://doi.org/10.2514/8.2520

[63] Cao, Y., Ma, C., Zhang, Q., and Sheridan, J., "Numerical Simulation of Ice Accretions on an Aircraft Wing," *Aerospace Science and Technology*, Vol. 23, Dec. 2012, pp. 296–304. doi: https://doi.org/10.1016/j.ast.2011.08.004

[64] Bourgault, Y., Boutanios, Z., and Habashi, W. G., "Three-Dimensional Eulerian Approach to Droplet Impingement Simulation Using FENSAP-ICE, Part 1: Model, Algorithm, and Validation," *Journal of Aircraft*, Vol. 37, May 2000, pp. 95–103. doi: https://doi.org/10.2514/2.2566

[65] Bourgault, Y., Beaugendre, H., and Habashi, W. G., "Development of a Shallow-Water Icing Model in FENSAP-ICE," *Journal of Aircraft*, Vol. 37, May 2000, pp. 640–646. doi: https://doi.org/10.2514/2.2646

[66] Papadakis, M., Hung, K. E., Vu, G. T., Yeong, H. W., Bidwell, C. S., Breer, M. D., and Bencic, T. J., "Experimental Investigation of Water Droplet Impingement on Airfoils, Finite Wings, and an S-Duct Engine Inlet," NASA/TM-2002-211700, 2002.

[67] Beaugendre, H., Morency, F., Habashi, W. G., and Benquet, P., "Roughness Implementation in FENSAP-ICE: Model Calibration and Influence on Ice Shapes," *Journal of Aircraft*, Vol. 40, May 2003, pp. 1212–1215. doi: https://doi.org/10.2514/2.7214

[68] Mineck, R. E., "Steady and Periodic Pressure Measurements on a Generic Helicopter Fuselage Model in the Presence of a Rotor," NASA/TM-2000-210286, 2000.

[69] Jang, J. S., Park, S. H., and Lee, D. J., "Prediction of Fuselage Surface Pressures in Rotor–Fuselage Interactions Using an Integral Solution of Poisson Equation," *Journal of the American Helicopter Society*, Vol. 59, Nov. 2014, pp. 1–11. doi: https://doi.org/10.4050/JAHS.59.042001

[70] Kenyon, A. R., and Brown, R. E., "Wake Dynamics and Rotor–Fuselage Aerodynamic Interactions," *Journal of the American Helicopter Society*, Vol. 54, Jan. 2009, pp. 12003–12003. doi: https://doi.org/10.4050/JAHS.54.012003

[71] Simcenter STAR-CCM+, Version 2022.1, Siemens, Germany, 2022.

[72] Lee, B.-S., Jung, M.-S., Kwon, O.-J., and Kang, H.-J., "Numerical Simulation of Rotor-Fuselage Aerodynamic Interaction Using an Unstructured Overset Mesh Technique," *International Journal of Aeronautical and Space Sciences*, Vol. 11, No. 1, 2010, pp. 1–9. doi: https://doi.org/10.5139/IJASS.2010.11.1.001

[73] Ruff, G. A., and Berkowitz, B. M., "Users Manual for the NASA Lewis Ice Accretion Prediction Code (LEWICE)," NASA Contractor Report 185129, 1990.

[74] Vargas, M., Papadakis, M., Potapczuk, M., Addy, H., Sheldon, D., and Giriunas, J., "Ice Accretions on a Swept GLC-305 Airfoil," *SAE Transactions 2002-01-1519*, 2002, pp. 58–71. doi: https://doi.org/10.4271/2002-01-1519

[75] Potapczuk, M., Papadakis, M., and Vargas, M., "LEWICE Modeling of Swept Wing Ice Accretions," *AIAA 2003-730*, 41st Aerospace Sciences Meeting and Exhibit, 2003. doi: https://doi.org/10.2514/6.2003-730

[76] Dubief, Y., and Delcayre, F., "On Coherent-Vortex Identification in Turbulence," *Journal of Turbulence*, Vol. 1, No. 1, 2000, Paper No. 011. doi: https://doi.org/10.1088/1468-5248/1/1/011